magnonic spectra on the detailed shape of antidots, promises the possibility for fabrication of high frequency magnonic waveguides with the current technology.

9. Two–Dimensional Magnonic Crystals

[*]Analogous to photonic crystals, magnonic crystals (MCs)[35,69,71] are magnetic meta-materials designed for the propagation of spin waves (SWs).[28,37,38,297] Based on their design, MCs exhibit a characteristic SW dispersion relation complete with bands and, sometimes, band gaps which can be tuned by controlling material and structural parameters as well as the strength and orientation of the bias magnetic field.[45,298] This phenomenon makes MCs useful as potential candidates for the design of SW based signal processing and logic devices.[299]

The knowledge of dispersion relation of a wave propagating through a medium is necessary to understand its transmission characteristics. Although MCs have been a subject of intense study lately,[49,50,52,58,68,79,83,86,213,300] reports on a time domain numerical calculation of dispersion relations of SWs propagating in two-dimensional (2D) MCs are very rare.[5,97,301] As other analytical methods are available, the use of time domain simulations and spatial Fourier transform to obtain the dispersion relation in a photonic or phononic crystal is rarely seen[302] as well. We hope to fill that gap in research with this work. The underlying principles, over which the procedure described here is used, has been discussed more generally in Chap. 4. Here too, we essentially use a micromagnetic simulator called Object Oriented Micromagnetic Framework[250] (OOMMF) to obtain magnetization $\mathbf{M}$, as a function of position $\mathbf{r}$, and time t. Then we use a multi-domain discrete Fourier transform to obtain the desired dispersion relation: SW power as a function of wavevector $\mathbf{k} = (k_x, k_y)$, and frequency f. However, while simulating the magnetization dynamics in large (ideally infinite[303]) 2D crystals, one can be expected to need far greater computational resources

[*]This chapter is based upon Kumar *et al.* *J. Appl. Phys.* **115**, 043917 (2014).

than during the simulations of their one-dimensional (1D) counterparts.[213] Using a finite sample size may produce some spurious modes in the obtained dispersion relation.[303] Thus, the use of 2D periodic boundary condition[244] (PBC) becomes mandatory in order to obtain good numerical resolution in wavevector and frequency domains while consuming finite computational resources. Also, 2D crystals have more high symmetry directions when compared to their 1D analogues. Different techniques will be required to obtain the results for different directions in the 2D reciprocal space covering the entire irreducible part of the Brillouin zone (BZ).[211] Moreover, the signal which generates the waves will have to be carefully designed so that the resulting spectrum represents the physical dispersion relation of plane propagating SWs. Due to all these complications, a need to validate the results obtained here with a well established method, such as the plane wave method (PWM)[51] becomes very clear.

The details of MC considered here are presented in sub–Sec. 9.1.1. Simulation parameters and PWM are described further in sub–Sec. 9.1.2. OOMMF uses the finite difference method (FDM) to solve the LLG equation as an ordinary differential equation in time and space (derivatives with respect to space are hidden away in $\mathbf{H}_{\text{eff}}$). PWM is based on the Bloch wave formalism. As these two methods are fundamentally different in approach, some quantitative differences in results are to be expected. The results from both the methods and their differences have been discussed in Sec. 9.2 for the antidot lattice (ADL). Due to small lattice constant, the considered system is an exchange dominated one and consequently, the differences in dispersion relations along the bias magnetic field and perpendicular to it are subtle. These differences have been explored by calculating the iso–frequency contours in the wavevector space using both MS and the PWM. The iso–frequency contours are the curves of the constant frequency plotted in the wavevector space, they are wave counterparts of the Fermi surfaces known from the theory of the solid state physics.[211] The iso–frequency contours are very important tool for the analysis of the wave propagation phenomena, giving a deep insight into direction and velocity of propagating, reflected and refracted waves in artificial crystals. Such type of analysis, while widely explored in photonic and phononic crystals for designing their metamaterials properties,[304–306] is almost absent in magnonics. Thus, developing the ability to compute these iso–frequency contours using MS can be a breakthrough in exploring magnonic metamaterials based on MC; because the MSs can be performed without approximation limited applicability of the PWM (or other analytical methods[245]), and thus yields experimentally realizable results even with complex magnetic configurations.

We also plot the energy spectral density and phase distributions associated with different modes in the SW spectrum in order to understand their physical origin and explain any observed partial or complete bandgaps. Finally, we use the method described here to obtain the SW dispersion relations in the case of 2D dot array where the SW propagation is mediated by inter-dot stray magnetic field as opposed to dipole-exchange interaction in ADL. This brings about an interesting change in the spectra, which is discussed in Sec. 9.2 along with their effective properties.

9.1. Method

9.1.1. Magnonic crystal lattice and material parameters

The structure considered here is an infinitely large square array of square antidots with their ferromagnet-air interface under pinned boundary conditions.[213] The geometrical structure of the sample is shown in Fig. 9.1 (a). The lattice constant $a = 30$ nm and the antidots are square holes of edge length, $l = 12$ nm. The material parameters of permalloy (Py: $Ni_{80}Fe_{20}$) are used during simulations and in PWM calculations: exchange constant, $A = 13\times10^{-12}$ J/m, saturation magnetization, $M_s = 0.8\times10^6$ A/m, gyromagnetic ratio, $\bar{\gamma} = 2.21\times10^5$ m/As and no magnetocrystalline anisotropy. A saturating bias magnetic field of $\mu_0\mathbf{H}_{\text{bias}} = 1$ T points in x direction.

9.1.2. Micromagnetic simulations and the plane wave method

The micromagnetic simulations involve solving the LLG equation using a finite difference method based ordinary differential equation solver; and then, Fourier transforming the obtained space and time dependent magnetization data to get SW spectral density in wavevector and frequency domains.[262] Cell size $(d, d, s) = (1.5, 1.5, 3)$ nm along (x, y, z) axis was used during the FDM based simulations. The pinning in micromagnetic simulations was

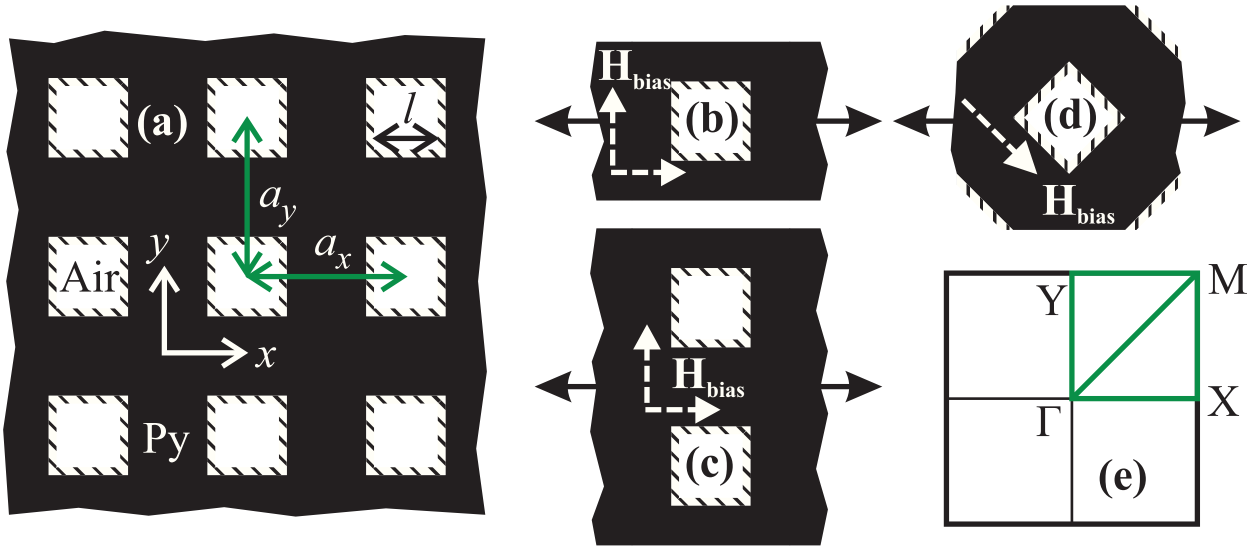

Figure 9.1.: (a) The 2D antidot lattice under consideration. A square lattice with a lattice constant $a_x = a_y = 30$ nm is assumed for simplicity. The thickness s of the film is 3 nm. The antidots are square (white) air holes of edge $l = 12$ nm in ferromagnetic Py (black) medium. Dynamics is pinned at the edge of holes. The pinned region is marked with a different texture. Element geometry used in micromagnetic simulations extends to over hundred repetitions in length (horizontal dark arrows in (b), (c) and (d)) for good wavenumber resolution. 2D PBC is applied over these elements to mimic the infinite geometry. White arrows in (b), (c) and (d) show the direction of bias field used for simulations of SW dispersion for BV and DE configuration. (d) shows the first BZ in the reciprocal lattice with typical symmetry point labels.

introduced by fixing magnetization vector in all cells of the discretization mesh, which border the antidots, i.e., in regions marked with different texture in Fig. 9.1. Figures 9.1 (b), (c) and (d) show parts of the elements over which 2D PBC are used to simulate the dispersion relation for different directions of the wave vector. These elements extend over 100 (up to 300) repetitions of unit cells in the horizontal direction to yield good resolution in the wavenumber domain. The 2D PBC is also implemented in order to improve the results with finite computational resources.[244] Figure 9.1 (e) shows the first BZ, the path in its irreducible part and typical symmetry points: $\Gamma = (0, 0)$, $\mathrm{X} = \pi/a(1, 0)$, $\mathrm{Y} = \pi/a(0, 1)$ and $\mathrm{M} = \pi/a(1, 1)$.[211] Note that when the bias field is in the plane, an asymmetry is expected between the two orthogonal directions of SW propagation: $\mathbf{H}_{\mathrm{bias}}||\mathbf{k}$ (BV) and $\mathbf{H}_{\mathrm{bias}} \perp \mathbf{k}$ (DE).[79] Thus, the triangle ΓXM is no longer the irreducible BZ. However, in the forward volume arrangement when $\mathbf{H}_{\mathrm{bias}}$ is perpendicular to the plane of the 2D MC, the symmetry is restored and dispersion is the same in the two orthogonal directions.[97,307] The technique described here can be used independent of the direction of $\mathbf{H}_{\text{bias}}$.

In order to get the results in the $\Gamma - \text{X}$ and $\text{Y} - \text{M}$ directions, we use different excitation signals of the form $\mathbf{H}_{\text{sig}} = (0, 0, H_z)$, on elements shown in Figs. 9.1 (b) and (c), respectively. $\mathbf{H}_{\text{bias}}$ is horizontal along the x axis (dashed white arrows). Similarly, dispersion along the $\Gamma - \text{Y}$ and $\text{X} - \text{M}$ directions can be obtained when $\mathbf{H}_{\text{bias}}$ is across the width of the elements (vertical arrows along y axis). Here, $H_z = H_0 N_t N(x) n_y$ with $\mu_0 H_0 = 5$ mT and N_t, $N(x)$ and n_y as given by Eqs. (9.1), (9.2) and (9.3), respectively:

$$N_t = \frac{\sin(2\pi f_{\text{c}}(t - t_0))}{2\pi f_{\text{c}}(t - t_0)}, \tag{9.1}$$

$$N(x) = \frac{\sin(k_{\text{c}} x)}{k_{\text{c}} x}, \tag{9.2}$$

$$n_y = \cos(2\pi y / y_{\text{max}}) + \sin(2\pi y / y_{\text{max}}). \tag{9.3}$$

See Eq. (7.2) for the detailed description of the terms involved in these equations. Here, the origin of coordinates is at the center of the considered geometry. It is due to N_t and $N(x)$ that the signal contains power between $\pm f_{\text{c}}$ and $\pm k_{\text{c}}$ in frequency and wavevector domains respectively.[262] n_y should be asymmetric to ensure that both symmetric and antisymmetric modes are present in the resulting spectrum.[297] In Eq. (9.3), y goes from 0 to y_{max}. While computing dispersion along $\Gamma - \text{X}$ and $\Gamma - \text{Y}$ directions (Fig. 9.1 (b)), $y_{\text{max}} = a$. However, for $\text{Y} - \text{M}$ and $\text{X} - \text{M}$ directions (Fig. 9.1 (c)), $y_{\text{max}} = 2a$. Both the elements in Figs. 9.1 (b) and (c) will span the same infinite 2D geometry under a 2D PBC; except, in the later case we can control whether the dynamics in the neighboring rows will be in phase or out of phase. Thus we can fix the wavevector component k_y or k_x to 0 or π/a in the simulations. This is necessary to differentiate between the parallel directions $\Gamma - \text{X}$ and $\text{Y} - \text{M}$ or $\Gamma - \text{Y}$ and $\text{X} - \text{M}$. Also, n_y^{mn} given by the expression

$$n_y^{mn} = C_m \cos(2m\pi y / y_{\text{max}}) + C_n \sin(2n\pi y / y_{\text{max}}) \tag{9.4}$$

can be used instead of n_y to selectively alter the amplitude of m-th symmetric or n-th antisymmetric mode. The freedom of choice of amplitudes C_m and C_n allows us to artificially control the statistical temperature of the magnons in the crystal and also helps in isolating a single mode in the case of a degeneracy. We can also sum over m and n to alter multiple modes in a single dynamic simulation. We also attempt to obtain the dispersion in $\Gamma - \mathrm{M}$ direction by using the element shown in Fig. 9.1 (d). However, as there are two scattering centres (antidots) per cell in this arrangement, we can obtain the dispersion relations correctly only up to half of the BZ in that direction.[97]

Until now, we could use a signal similar to the one we did in the case of an 1D lattice.[68] But, this limitation forced us to come up with a new signal

$$H_z = H_0 N_t N(x) N(y) n(x) n(y), \tag{9.5}$$

which has to be used in a larger 2D lattice of 100×100 antidot array (with the cell size d increased to 3 nm to decrease time of computations). Here, $n(x)$ is given by:

$$n(x) = \sum_{m=1}^{5} \left(\sin(2\pi m x/a) - \cos(2\pi m x/a) \right), \tag{9.6}$$

with analogous formula for $n(y)$. This signal is a point like source with the amplitude decay with distance as described by sinc function (in $N(x)$ Eq. (9.2) along x axis and in similar form for $N(y)$ for y dependence), having sharp cut-off in Fourier domain and able to excite symmetric and antisymmetric modes with respect to $x-$ or $y-$ axis. This signal was arrived upon largely by intuition, nevertheless, its agreement with the results obtained from PWM validates the usefulness of this signal. Spectral density, periodicity and asymmetry of the excitation signal (or source) should also be considered while developing similar techniques for other kinds of crystals (*e.g.* photonic or phononic crystals).

Three fold (one in time and two in space) Fourier transforms was needed to obtain the SW dispersion here. Magnetization was assumed to be uniform across the thickness of the film. We can now easily generalize that in the case of three-dimensional MCs, a signal of the form $H_z = H_0 N_t N(x) N(y) N(z) n(x) n(y) n(z)$ will be required followed by a four fold discrete Fourier transform.

We have also calculated the spatial distribution of energy spectral density (ESD), S_f and phase, θ from the following equations:

$$S_f = |\tilde{m}(\mathbf{r}, f)|^2; \tag{9.7}$$

$$\theta = \tan^{-1}\left(\frac{\mathrm{Im}\left(\tilde{m}(\mathbf{r}, f)\right)}{\mathrm{Re}\left(\tilde{m}(\mathbf{r}, f)\right)}\right). \tag{9.8}$$

Here, $\tilde{m}(\mathbf{r}, f)$ is the time domain Fourier transform, of a dynamical magnetization data. Unlike the new method used in Chap. 7, this gives us power from the entire wavevector domain for a selected frequency f. However, if power is present for just one particular wavevector then both methods yield qualitatively identical results.

The PWM is a spectral method in which the eigenproblem is numerically solved in the frequency and wavevector domains by the standard numerical routines. We solve here LLG equation in linear approximation without damping. The PWM calculations are performed with the assumption of the full magnetic saturation of the ADL along the bias magnetic field. As pinning during simulation will occur at the cell's center, a hole size of $l + d$ was assumed during PWM calculations. Due to small thickness of the ADL, uniform SW profile across the thickness is assumed. The PWM in this formulation was already used in the calculations of the SW dynamics in 2D ADL and proved to give correct results.[4,57,62,213] The detailed description of the method can be found in Refs. 62 and 308.

9.2. Results and Discussions

The dispersion along the path in the first BZ shown in Fig. 9.1 (e) calculated with MSs by using the elements shown in Fig. 9.1 (b)-(d) is assembled as Fig. 9.2 (a) using solid lines. An overlay of dashed lines representing the SW dispersion relation obtained from the PWM is provided for comparison. Both these results appear to agree with each other except for the $\Gamma - \mathrm{M}$ direction where the numerical method was able to yield results for only half of the total BZ extent. This is because we set k_c to $\pi/\left(\sqrt{2}a\right)$ here (the spatial periodicity is $\sqrt{2}a$). Compared to the element shown in Fig. 9.1 (b), which can be used to produce results for $\Gamma - \mathrm{X}$ or $\Gamma - \mathrm{Y}$ directions, the one in Fig. 9.1 (d) features two scatter centres per unit cell. And, if we artificially increase k_c to $\sqrt{2}\pi/a$, both scattering centres will be activated to produce additional spurious modes.[97] To demonstrate the same we plot S_f (normalized

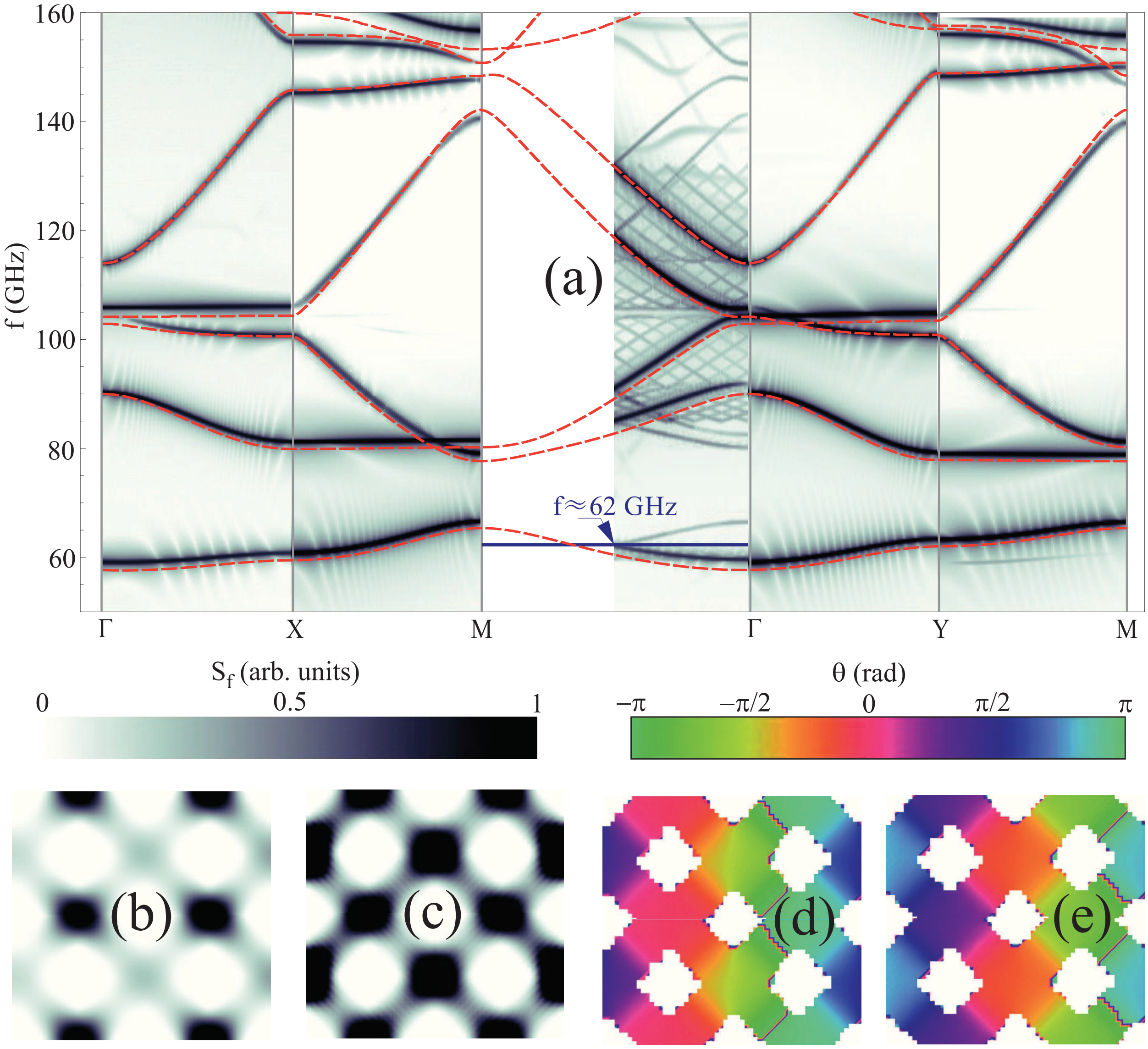

Figure 9.2.: (a) SW dispersion calculated using MSs (solid line) and PWM (dashed lines). ESD S_f, distribution for the horizontal line ($f \approx 62$ GHz) shown in (a) in parts of the sample when the propagation direction is along $\Gamma - \mathrm{M}$ for (b) $k_\mathrm{c} = \pi/\left(\sqrt{2}a\right)$ and (c) $k_\mathrm{c} = \sqrt{2}\pi/a$. Corresponding phase θ, distribution is shown in (color online) (d) and (e), respectively.

between 0 and 1) and θ (given by Eqs. (9.7) and (9.8), respectively), for frequency $f \approx 62$ GHz in Figs. 9.2 (b) to (e). Note that the horizontal separation between regions of high ESD is about $\sqrt{2}a$ in Fig. 9.2 (b) for $k_\mathrm{c} = \pi/\left(\sqrt{2}a\right)$. This reduces to $a/\sqrt{2}$ in Fig. 9.2 (c) for $k_c = \sqrt{2}\pi/a$ when both scattering centres in the unit cell (of the element shown in Fig. 9.1 (d)) are activated at once. The phase distributions also confirm that neighbouring locations of high ESD are about π and $\pi/2$ radians out of phase with each other in former

($k_c = \pi/\left(\sqrt{2}a\right)$: Fig. 9.2 (d)) and later ($k_c = \sqrt{2}\pi/a$: Fig. 9.2 (e)) cases, respectively. Apart from incomplete result for the $\Gamma - \mathrm{M}$ direction, we can also see that the modes here (shown by solid lines) do not match with those for $\Gamma - \mathrm{Y}$ direction at the Γ point. This is because (cell size) $d = \sqrt{2}$ nm was used while simulating for the $\Gamma - \mathrm{M}$ direction as opposed to $d = 1.5$ nm, which was used in the case of $\Gamma - \mathrm{Y}$ direction. Also, there are additional modes of lower amplitudes visible in the case of $\Gamma - \mathrm{M}$ direction. This is due to the fact that $N(x)$ becomes a stepped approximation of the right hand side of (9.2) by the use of the FDM; thus compromising the effectiveness of the cut off at $k_c = \pi/\left(\sqrt{2}a\right)$, and exciting the second scattering centre to some extent (but not as well as $k_c = \sqrt{2}\pi/a$).

In pursuit of our quest to close the gap in the $\Gamma - \mathrm{M}$ direction we eventually decided to simulate the SW dynamics in a large 2D MC with signal defined by Eq. (9.5) and perform a three-fold Fourier transform in contrast with the two-fold transforms done earlier. We transformed time to frequency domain and $x-$ and $y-$ dimensions to the 2D wavevector domain. The resulting dispersion relation as calculated from the numerical method is shown in Fig. 9.3 (a) using solid lines. Thus, we have obtained the magnonic band structure along all high the symmetry directions. The overall agreement with the PWM results (shown by dashed lines) although is poorer in comparison with Fig. 9.2 (a). This is due to the fact that cell size in the later attempt was increased from $d = 1.5$ nm to $d = 3$ nm. The complete and partial bandgaps width and center frequency, as seen from the dashed lines in Fig. 9.3 (a), are extracted in Tab. 9.1. Here, values for partial bandgaps depend upon the path, which has been used to plot the dispersion. Bandgap I is the only complete bandgap observed here with the maximum width of 15.37 GHz.

Most bands observed in Fig. 9.3 (a) increase or decrease almost monotonously along any high symmetry direction. Consequently, the width of bandgap I too, appears to decrease monotonously as we move either along $\Gamma \to \mathrm{X} \to \mathrm{M}$ or $\Gamma \to \mathrm{Y} \to \mathrm{M}$. Both upper and lower limits of bandgap I are present at point M which suggests an anti-crossing of bands at that point. This can also be regarded as the cause of the gap formation. Narrower bandgap widths have been observed by different techniques before.[60] The relatively high width of 15.36 GHz of bandgap I here can be attributed to small lattice dimensions and edge pinning.[213] Bandgaps II to XI (Fig. 9.3 (a) and Tab. 9.1) are direction dependent partial bandgaps.

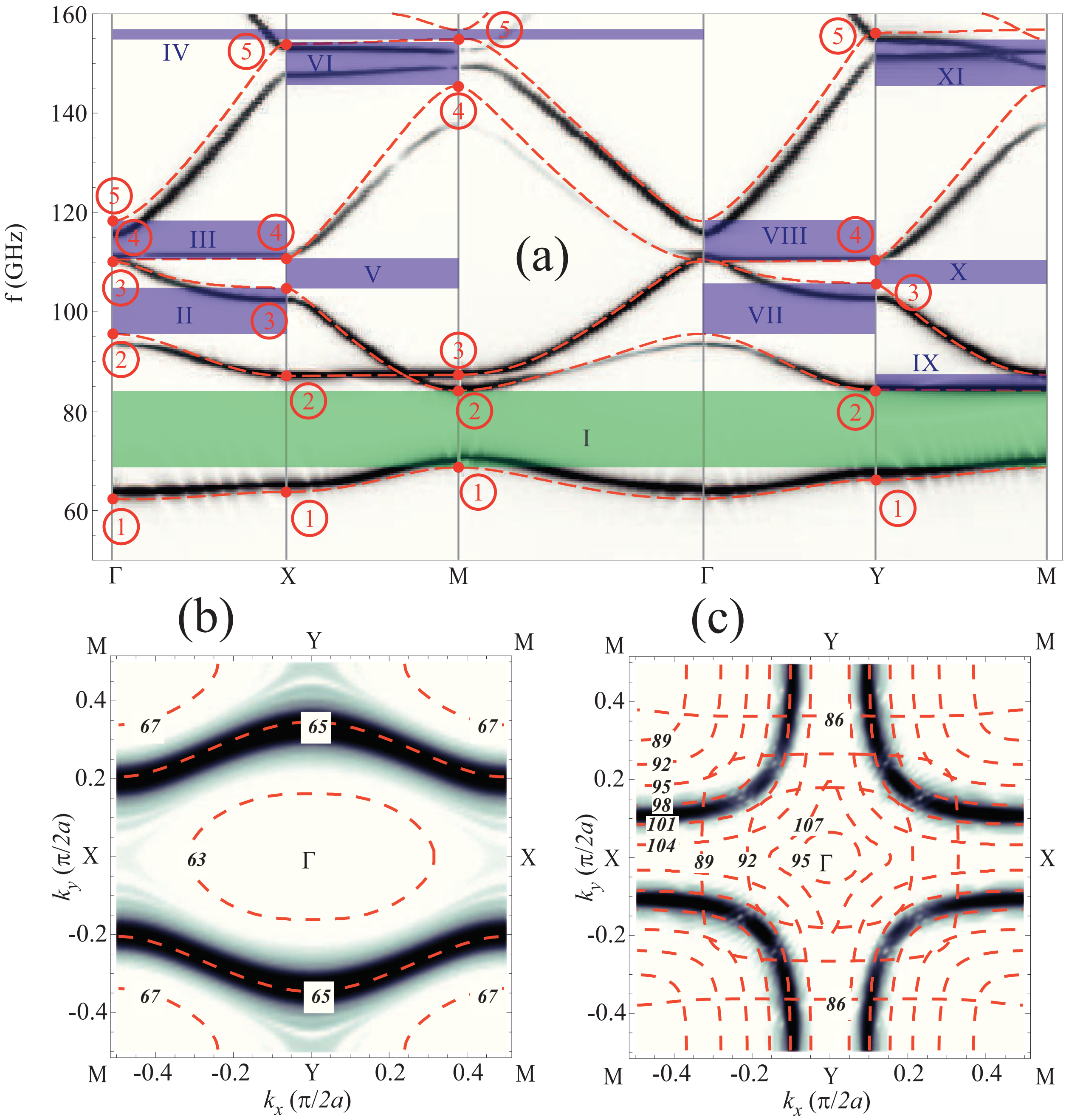

Figure 9.3.: (a) SW dispersion calculated using MS (solid line) and the PWM (dashed lines). The full and partial magnonic bandgaps are marked and numbered by Roman numerals. The circled Arabic numerals indicate the points on the dispersion for which the mode profiles are calculated in Fig. 9.4. Iso–frequency lines from (b) 63 GHz to 67 GHz (c) 86 GHz to 107 GHz (it is around the top and bottom of the first and second magnonic band, respectively) using the PWM is shown with dashed lines. Iso–frequency lines for (b) $f \approx 67$ GHz and (c) $f \approx 100$ GHz calculated by the numerical method is shown using solid lines.

Table 9.1.: Magnonic bandgap widths and center frequencies across different high symmetry directions as calculated by the PWM and labeled in Fig. 9.3 (a).

Label	Extent	Center (GHz)	Gap Width (GHz)
I	Complete Bandgap	76.39	15.36
II	$\Gamma - X$	100.18	9.24
III	$\Gamma - X$	114.45	7.7
IV	$\Gamma - X - M - \Gamma$	155.85	1.9
V	$X - M$	107.75	5.9
VI	$X - M$	149.6	8.4
VII	$\Gamma - Y$	100.68	10.24
VIII	$\Gamma - Y$	114.2	8.2
IX	$Y - M$	85.80	3.01
X	$Y - M$	108.1	4.6
XI	$Y - M$	150.1	9.4

This is mainly because bands approaching point M from other high symmetry directions (with the exception of the band starting at Γ⑤) tend to show greater slopes. As X⑤→ Y⑤ is a relatively flatter line, bandgap IV survives for three high symmetry directions. In a more isotropic forward volume arrangement,[97,307] bandgap IV might also have qualified as a complete bandgap if the dispersion in the $X-M$ direction was also calculated. On the other hand, if wavevector dependent anisotropy is overlooked,[5] partial bandgaps (e.g. bandgap IV, or II and VII, or III and VIII) will appear as a complete bandgap. Partial bandgaps IV, V, VIII, X and XI are direct, while II, III, VI, VII and IX are indirect. Direct bandgaps are formed when the minimal and the maximal frequency of the magnonic bands surrounded the bandgap, from the top and bottom, respectively, are characterized by the same wavevector. While two different wavevectors are involved in the formation of indirect bandgap. In Fig. 9.3 (a) the minimal and maximal frequencies appear at high symmetry points. Occasionally, a bandgap may form between two high symmetry points due to anti-crossing of modes in a folded BZ,[4] but that is not observed here.

Now we calculate mode profiles ESD S_f and phase θ, at the high symmetry points, using the PWM, for the first five modes as marked in Fig. 9.3 (a). The results are tabulated as Fig. 9.4 where S_f is represented by colour saturation and θ is represented by hue. A general trend of higher frequency mode profiles limiting themselves to smaller regions in real space is observed. This trend has been seen for 1D systems as well.[4] Here, mode profiles

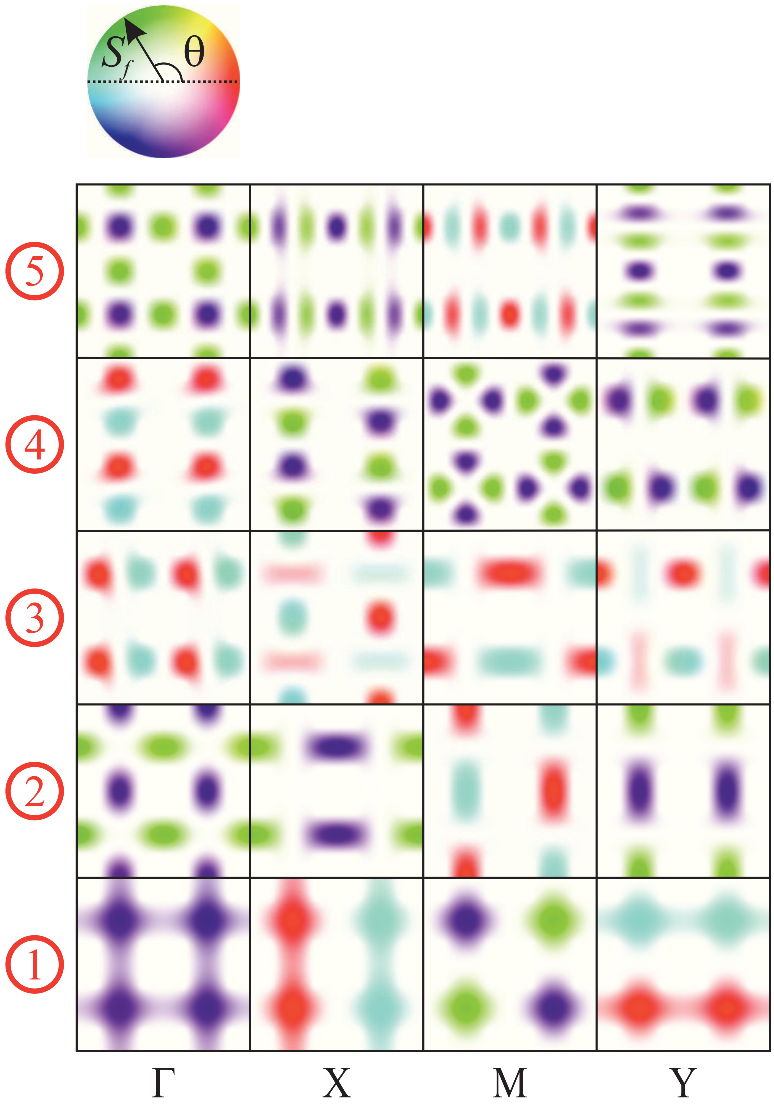

Figure 9.4.: (Color online) ESD S_f, and phase θ, for high symmetry points Γ, X, M and Y at points ① through ⑤ marked on Fig. 9.3 (a).

appear similar in size at points X⑤, M⑤ and Y⑤. Although, the distribution at Y⑤ is vastly different due to a (nearby) mode–crossing in the Y − M direction (see Fig. 9.3 (a)). Mode profile at Y may be obtained by rotating the mode profiles at X by 90°. Modes with negligible group velocity are trapped and forbidden to move in specific high symmetry directions. Also, the number of nodal lines, which controls the spatial quantization of modes, generally increases with mode number ⓘ: $i \in \{1, 2, 3, 4, 5\}$. No nodal lines are evident for Γ①. Vertical and horizontal nodal lines are seen at X① and Y①, respectively; while M① features both vertical and horizontal nodal lines. From Fig. 9.3 (a), we can see that points Γ②, X②, M③ and Y③ belong to the same mode and points Γ③, X③, M② and Y② belong to a different mode. As the crossing between these modes occurs along the $X - M$ direction, the mode profiles at X② and M③ are comparable. Similarly, mode profiles at X③ and M② are also comparable except, X③ has higher frequency and consequently, is more confined is space. In general, vertical and horizontal nodal lines dominate at points X and Y, respectively; while a more isotropic distribution is observed at point Γ and M. Modes ①, ②, and ⑤ are isotropic along $x-$ and $y-$axes for the Γ point. However, modes ③ and ④ are disposed along rows and columns, respectively. Their local shape and size are comparable and accordingly, they are also degenerate as seen in Fig. 9.3 (a). Going from Γ to either X or Y, ④ maintains its size and frequency; except the DE[309] geometry is evident in the later case. Similarly, the expanses of mode profiles at M② and ③ are comparable (as their frequencies are within 5 GHz of each other), and yet their orientations are mutually orthogonal.

Iso–frequency lines are shown in Figs. 9.3 (b) and (c), using both the PWM (dashed lines) and the MSs (solid lines). Iso–frequency contours calculated using the proposed method are thicker because small a yields a low wavevector resolution. The agreement between the results obtained from the two methods as 67 GHz line calculated using the MSs and the 65 GHz line calculated using the PWM is clear, but the 2 GHz difference in frequencies is due to the shift of the dispersion curves calculated with both methods shown in Fig. 9.3 (a). In contrast to Fig. 9.3 (b) the two methods appear to give identical results for the 100 GHz iso–frequency line, where the results of MS and PWM coincide. The shapes of iso–frequency lines control the direction of the propagating waves and consequently also alter the shapes of their wavefronts. Thus, although the dispersion along $\Gamma - X$ and $\Gamma - Y$ directions may appear comparable, the wavefronts of the propagating SWs from the first band will quickly uncover the underlying anisotropy, because of slightly different group velocity and curvature of different iso–frequency contours in two orthogonal directions, which is easily noticeable by the inspection of the contours for 63 and 65 GHz in Fig. 9.3 (b). This anisotropy is a manifestation of dipolar interactions hardly visible in this size and frequency regime in the magnonic band structure shown in Fig. 9.3 (a). Backward volume modes are characterized by negative group velocity in the case of dipole dominated or dipolar-exchange SW propagating in a ferromagnetic thin film.[28] This is not seen in Fig. 9.3 (a) as due to weakness of the dipolar interactions the exchange field makes a significant contribution with increasing wavevector **k** already near the BZ center.

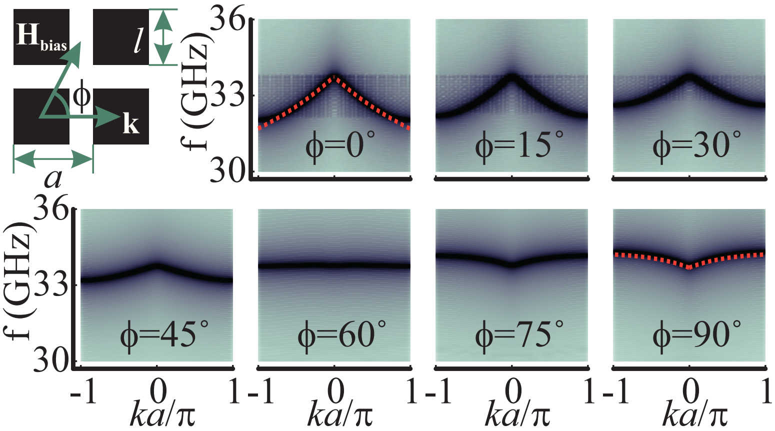

Figure 9.5.: First mode in a permalloy nano–dot array with varying angle ϕ, between the bias field $\mathbf{H}_{\text{bias}}$ ($\mu_0\mathbf{H}_{\text{bias}} = 1$ T), and wavevector **k**, showing the transition from magnetostatic BV mode to DE configuration. The dashed lines are calculated using the analytic expressions for these two configuration with a reduced saturation magnetization. The structure considered here is given in the top left corner with $a = 9$ nm, $l = 6$ nm and thickness $s = 3$ nm. Material parameters remain the same as before.

The developed method is not limited to the antidot lattices nor exchange dominated SWs. To prove this and better understand the properties of dipolar waves in MCs we take a look at the dispersion of SWs in the case of 2D MC composed of a square array (of lattice constant $a = 9$ nm) of square dots (of edge $l = 6$ nm and 3 nm thick). This structure is shown in the top left panel of Fig. 9.5 along with the dispersion relations of the first mode with increasing angle ϕ (from $\phi = 0$ to $\phi = 90°$), between $\mathbf{H}_{\text{bias}}$ and **k** in the subsequent panels. Here the wave propagation is mediated by the dipolar field only. We have found a strong anisotropy in the spectrum of the collective magnetostatic SW excitation, similar to already observed in the arrays of ferromagnetic dots of larger size in Ref. 47. We note here how the mode's group velocity gradually increases from negative (BV) to positive (DE) as ϕ goes from 0° to 90°.[47,301] The transition appears to occur at a critical angle $\phi = \phi_{\text{c}} \approx \pi/3$. Note that here the direction of $\mathbf{H}_{\text{bias}}$ is being changed as opposed to that of **k** in the previous case. It is interesting to note that the dispersion relations obtained here for the array of nano–dots reminds us of the dispersion of magnetostatic waves in thin ferromagnetic film. To verify this hypothesis we calculate the dispersion relation of magnetostatic waves in the thin ferromagnetic magnetic film (3 nm thick) with reduced magnetization, *i.e.* with the effective value of the saturation magnetization $M_{\mathrm{s,eff}}$. The dashed lines overlaid in Fig. 9.5 are computed using the analytical expression for BV and DE configuration in the case of thin film[28] with a reduced saturation magnetization $M_{\mathrm{s,eff}} = M_{\mathrm{s}} l^2/a^2$. A good agreement between the dispersion in the array and the effective thin film is found. A minor disagreement is introduced by the presence of the BZ boundaries but only near these boundaries. Further, the critical angle, $\phi_{\mathrm{c}} = \tan^{-1}\sqrt{H_{\mathrm{bias}}/M_{\mathrm{s,eff}}}$[310] in the case of such thin film is also $56.24° \approx \pi/3$. This implies that one should also be able to use the analytical expression to calculate the SW manifold between BV and DE geometries. This also shows, that a thin film MC composed of an array of saturated ferromagnetic nanodots can be used as a magnonic metamaterial, i.e., an artificial crystal with tailored effective properties of spin wave dynamics.[311–314] Further studies are necessary to elucidate the limits of the effective saturation magnetization approach presented here. The influence of the dot–shape, their arrangement and inter–dot separation (mode-splitting has been experimentally demonstrated for nano–dot arrays[315]) need to further examined. However, these considerations are outside the scope of this work.

9.3. Conclusions

We have described a numerical algorithm to calculate the dispersion of plane propagating SWs in a 2D MC using multi-domain Fourier transform of results obtained from micromagnetic simulations. At the core of this technique is a new excitation signal, which is capable of generating SWs whose energy spectral density corresponds to the characteristic dispersion relation of the 2D MC. The lack of such signal has been discussed before in the case of 1D MCs.[270,271] The results obtained from this procedure were verified by the plane wave method when magnetization dynamics at antidot boundaries is pinned. We noted that both methods were in qualitative agreement with each other. The fact that better quantitative agreement was observed while using 2D PBC over 1D elements was due to lower cell size.[4]

Apart from a new numerical algorithm to compute the dispersion relation in any given direction of a two- or three-dimensional inverse lattice, this method will also allow for the numerical computation of iso–frequency contours from micromagnetic simulations. Thus the numerical tool to study metamaterials properties of MCs was provided. It gives the possibility to design the properties of SWs relevant to technological applications and potentially exceeding these known from the homogeneous ferromagnetic thin films. The negative refraction, unidirectional media or caustic propagations are only some of the examples here.[195,316,317] Further, this method can be generalized to aid the numerical computation of dispersion or iso–frequency contours in the case of two– or three–dimensional phononic[318] and photonic[319,320] crystals as well.

The dispersion here appeared to be similar in $\Gamma - \mathrm{X}$ and $\Gamma - \mathrm{Y}$ directions. However, a noticeable anisotropy between the BV and DE geometries was very evident from the study of the mode profiles and the iso–frequency contours. As dipole field mediates the SW propagation in a 2D dot array we were able to obtain the negative group velocity associated with the first mode in the case of a BV magnetostatic configuration. We were also able to analyse the nature of bands and complete and partial bandgaps that were obtained from the dispersion calculations in the case of an MC. This can be useful in the design of attenuators,[321] phase–shifters,[83] filters[85] and logic gates.[77]

Low lattice constants were chosen in this article for both the antidot and the dot lattices to ensure a realistic computational time within the available computational resources. For larger lattice constants, larger cell sizes may be used with OOMMF. Cell sizes should not exceed the exchange length (about 5.6 nm in Py), if the exchange interaction is to be taken into account. In the case of 1D antidot waveguide, we noted[66] that a larger value of lattice constant a, brings the BZ boundaries closer and makes the modes less dispersive. Thus a smaller value of $a = 9$ nm is used in the case of the nanodot array. In Ref. 47, some dispersion is observed (particularly in DE configuration), as nanodots are 30 nm thick. Simulating for a structure which is ten times thicker will similarly increase the required computational time. Recent advances in lithography techniques[50,98–100] have made it possible to fabricate dot and antidot lattices with a resolution below 10 nm. Thus, one can fabricate samples with dimensions comparable to the systems considered here. Experimental techniques similar to Brillouin light scattering spectroscopy[111] can be used to explore the SW dispersion relation.

The details of chapter 10 (pages 145 to 150) cannot be made public at present.

11. Experimentation Involving Magnonic Antidot Waveguides

In this chapter, we discuss the some experimental results following the numerical works presented on one–dimensional (1D) magnonic antidot waveguides (MAWs). However, even with the recent advancements in nanofabrication, it is still not possible to fabricate large 1D or 2D periodic arrays of fine features with great precession. The samples presented here were fabricated using lithography techniques discussed in Sec. 3.5.

11.1. MAW Samples

The generic form of samples fabricated for this study is described in Fig. 11.1. The length and width of the waveguide was approximately $60\,\mu$m and $5\,\mu$m, respectively. Thickness was about 20 nm. Circular antidots of diameter d were milled in a 6×30 array placed close to the middle of this waveguide. Their edge to edge separation was a_x along the length. The separation, a_{yi} between i^{th} and $(i+1)^{\text{th}}$ row is given as

$$a_{yi} = \begin{cases} a_{y1} & \text{i is odd} \\ a_{y2} & \text{i is even} \end{cases} . \tag{11.1}$$

Four such samples were studied experimentally using a time–resolved magneto–optic Kerr effect (TR–MOKE) setup. The approximate values of the parameters used for these samples are tabulated in Tab. 11.1. The exact values of antidots' diameters and their edge–to–edge separations (a_x, a_{y1} and a_{y2}) are within 10% of the tabulated values. Henceforth, the samples will be referred to by their Sample IDs as given in the table.

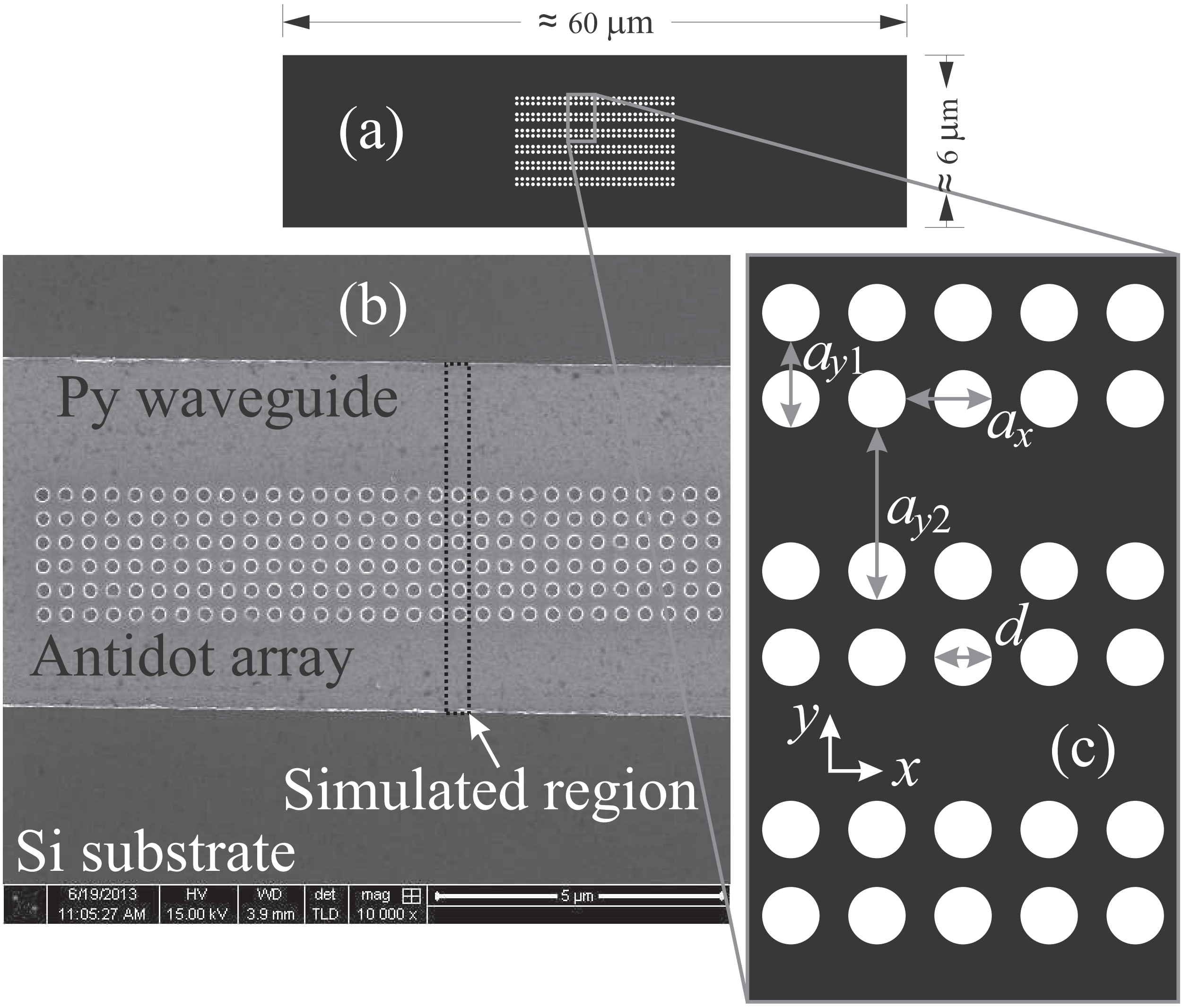

Figure 11.1.: (a) Dimension of the Py waveguide in which antidots were milled using focused ion beam lithography. (b) A scanning electron microscopy image produced during the inspection of the fabricated sample showing the 20 nm thick Py waveguide along with the antidot array, deposited over the Si substrate. (c) Dimensions within the antidot array.

Table 11.1.: Assignment of sample IDs to an instance of geometrical parameters as labelled in Fig. 11.1.

Sample ID	d **(nm)**	a_x **(nm)**	a_{y1} **(nm)**	a_{y2} **(nm)**
①	180	410	410	410
②	210	410	430	320
③	210	330	320	320
④	210	520	550	550

11.2. Magneto–Optic Kerr Effect (MOKE)

MOKE is a type of magneto–optic interaction associated with the change in polarization of light reflected from a magnetized surface. This effect was first observed by John Kerr in 1877.[322] The interaction of light with the applied magnetic field and magnetization of the material has been theorized to be the cause of this effect.[6] Upon reflection from a magnetized surface, a linearly polarized light transforms to an elliptically polarized light where the major axis of the ellipse is rotated from the plane of polarization of incident light by an angle proportional to the magnetization. This angular deviation can be measured to estimate the magnetization.

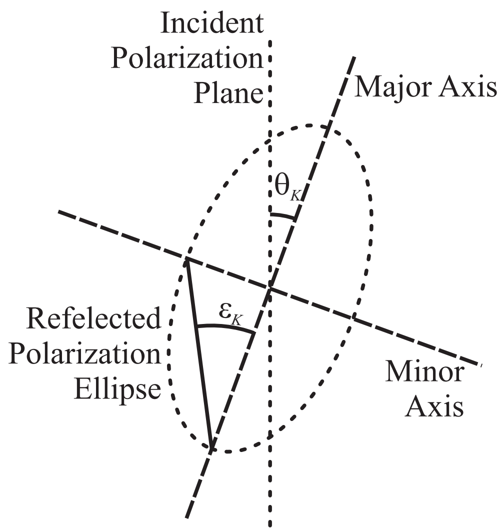

Figure 11.2.: Incident polarization plane and reflected polarization ellipse shown in dotted lines. Major and minor axes of the ellipse are shown in dashed lines. Kerr rotation and ellipticity are represented by angles θ_K and ϵ_K, respectively.

The angular distance between the major axis of the ellipse (of the elliptically polarized reflected light) and the plane of polarization (of the plane polarized incident light) is define as *Kerr rotation*. This is marked as angle θ_K in Fig. 11.2. *Kerr ellipticity* measures the flatness of the ellipse and is represented by angle ϵ_K in Fig. 11.2. In our experiments we are interested in the Kerr rotation signal only.

11.2.1. Description of The Pump–Probe Optical Setup

A schematic of the TR–MOKE setup is presented in Fig. 11.3.[6] This setup is mounted on an optical table which is engineered to facilitate rapid attenuation of any acoustic vibrations. The table also features a very smooth surface covered with a square array of circular holes (25 mm grid) which facilitates the equipment setup process.

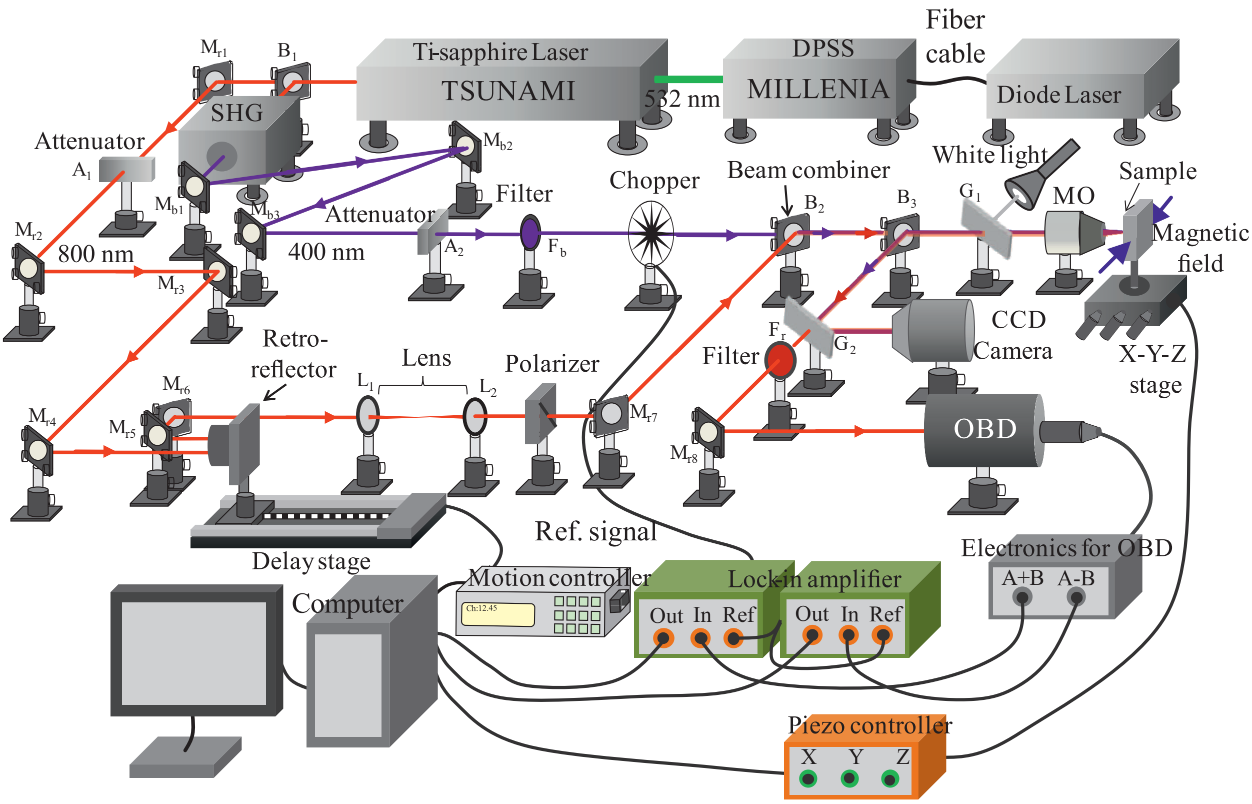

Figure 11.3.: A schematic diagram of an all optical TR–MOKE microscope with collinear pump–probe geometry as housed in the lab at the S. N. Bose National Centre for Basic Sciences. Source: Ref. 6.

As seen in Fig. 11.3, a diode laser is used to pump a solid state laser (Millenia), which in turn pumps the Ti–sapphire laser (Tsunami) with a maximum power of 10 W using a 532 nm light. Regenerative mode locking is used here to produce a train of laser pulses with $\approx$ 70 fs pulse width and average power of $\approx$ 1.6 W. The pulses come at a frequency of 80 MHz ($\approx$ 20 nJ/pulse). The output of a Ti–sapphire laser can be tuned from 690 nm to 1080 nm. However, here we keep the output wavelength at 800 nm. The Tsunami laser features control knobs which manipulate prisms in optical path to change the mean wavelength, pulse-width and power of the output beam. This output beam is vertically polarized with a spot size of

≈ 2 mm.

About 70% of the beam is directed towards a second harmonic generator (SHG) using the beam splitter B_1 (see Fig. 11.3). An SHG uses non–linear methods[323] to halve the beam wavelength to 400 nm. This beam is used to excite the magnetization dynamics and is referred to as the *pump beam*. The Kerr rotation and thus the magnetization dynamics is probed using the 800 nm beam. This is referred to as the fundamental beam or the *probe beam*. The paths of the pump and probe beams are marked by blue and red lines, respectively in Fig. 11.3. A spectral filter F_b is used to ensure that no trace of the fundamental beam remains mixed with the probe beam. A sequence of mirrors (M_{b1}, M_{b2} and M_{b3}) is used to guide the pump beam on to the sample. An attenuator is used to control the intensity of the incident pump beam. A chopper modulates the intensity of the pump beam at 2 kHz. This modulation frequency also serves as a reference signal during the lock–in detection process of the probe beam. The path of the pump beam remains fixed.

The probe beam passes through a computer controlled variable delay stage, which uses a retro–reflector to turn the beam by 180° with some lateral off–set. Fixed mirrors (M_{r1}, M_{r2}, M_{r3} and M_{r4}) are used to guide the probe beam on to the retro–reflector. An attenuator is also used here to control the intensity of the probe beam. Mirrors M_{r5}, M_{r6} and M_{r7} are used to guide the retro–reflected probe beam on to the sample. A pair of collimating lenses L_1 (focal length = 75 nm) and L_2 (focal length = 200 nm) are used in telescopic arrangement to increase the probe beam's diameter to ≈ 5 mm, so the entire back–aperture of the microscope objective (MO) may be used. A Glan–Thompson polarizer (extinction coefficient $100,000 : 1$) is used to refine the polarization state of the probe beam.

Both pump and probe beams are combined at beam combiner B_2, which is essentially a $50 : 50$ non–polarized beam splitter set at 45° to the optical of the probe beam. Meticulous effort is required to ensure that both the pump and the probe beams remain collinear from this point.[6] The combined beam then passes through a MO (M–40X; N. A. = 0.65) at normal incidence which focuses the probe beam on the surface of sample to a diffraction limited spot size of about 800 nm. The pump beam is slightly defocused (spot size = 1μm) on the sample due to chromatic aberration. The sample is held by using a sample holder mounted on a computer controlled piezoelectric scanning $x - y - z$ stage.

A white light source is used to illuminate the surface of the sample. This helps see micron size features on the sample using a charged coupled diode (CCD) camera and ascertain that the pump and probe beams are aligned on a desired spot on the sample. White light from the white light source is reflected into the MO by using a glass slide (G_1). A beam–splitter B_3 is used to turn the reflected pump, probe and white lights by 90° (see Fig. 11.3). The white light is guided into the CCD camera by using another glass slide (G_2). The white light is turned off once the initial alignment has been verified. The probe is filtered out using a spectral filter F_r. Thus only the reflected probe beam, which contains the Kerr rotation signal is allowed to reach the optical bridge detector (OBD). Due to the conical symmetry of the beam focused using the MO, the effect of the in–plane (longitudinal and transverse) components of magnetization gets averaged out and only the out of plane, or *polar* component of magnetization contributes to the observed Kerr rotation.

Within the OBD, a polarized beam–splitter is used to split the elliptically polarized reflected probe beam into two mutually orthogonal plane polarized beams. The intensity of these plane polarized beams is converted into electronic signals, A and B, using Si–photodiodes. The sum $(A+B)$ and difference $(A-B)$ of these signals give total reflectively and Kerr rotation. The polarized beam–splitter is kept at 45° to the initial plane of polarization to ensure the *balance* of the bridge: $A-B=0$. Generally, $A-B \propto M_z$, where M_z is the $z-$ component of the magnetization. The reflectivity signal $(A+B)$, contains information regarding carrier dynamics and phonon dynamics.

11.3. Results and Discussion

11.3.1. TR–MOKE Measurements from the $Ni_{80}Fe_{20}$ Antidot Waveguide

Figure 11.4 shows the time–resolved Kerr rotation and the corresponding spin wave spectra and the simulation data corresponding to ① in (top panels) backward volume (BV) and (bottom panels) Damon–Eshbach (DE) configurations (see sub–Sec. 2.4.2). The Kerr rotation signals $\theta_K \propto A - B \propto M_z$ as obtained from TR–MOKE microscopy for BV and DE configurations is given in Figs. 11.4 (a) and (b), respectively. Here the BV and DE configurations refer to arrangements where the bias magnetic field is applied along $x-$ and $y-$ axes of the geometry described in Fig. 11.1 (c). In both cases, an ultrafast demagnetization followed by a fast re-magnetization and a slow re-magnetization and a precessional oscillation superposed on the relaxing magnetization is observed. A bi–exponential background (see sub–Sec. 2.3.4) is subtracted from the raw data to obtain θ'_K:

$$\theta'_K(t) = \theta_K(t) - \theta_1 \exp(-t/\tau_1) - \theta_2 \exp(-t/\tau_2). \tag{11.2}$$

Here t is the time delay (controlled by the delay stage) in the arrival of the probe (beam) pulse w.r.t. to the pump (beam) pulse. $\theta'_K(t)$ is shown for BV and DE configurations in Figs. 11.4 (c) and (d), respectively. The variables θ_1, θ_2, τ_1 and τ_2 are obtained using curve fitting techniques while minimizing the standard deviation of $\theta'_K(t)$. τ_1 and τ_2 are the relaxation times as discussed in sub–Sec. 2.3.4. The values of τ_1 and τ_2 obtained from curve fitting the experimental data presented in this chapter are of the order of 5 ps and 200 ps, respectively. Uniform waveguides registered a higher value of τ_1 ($\approx$ 10 ps). These results are in agreement with known values for permalloy.[6]

Energy spectral densities (ESDs) – squares of Fourier transforms of $\theta'_K(t)$ for BV and DE configurations are plotted in Figs. 11.4 (e) and (f), respectively in arbitrary units using a non–logarithmic scale. Figs. 11.4 (g) and (h) are ESDs obtained using micromagnetic simulations for BV and DE configurations, respectively. The material parameters of Py were used during simulation with a cell size of 5 nm $\times$ 5 nm $\times$ 20 nm. A Gilbert damping constant of 0.008 was used for the dynamic simulation. A pulse excitation field was used to trigger the magnetization dynamics. Here the Fourier transforms are done directly on the spatially averaged $z-$ component of magnetization. 1D periodic boundary condition (PBC) is used on a column of holes (as shown in Fig. 11.1)to mimic a large array. The same material parameters of Py, as used in the previous chapters (see page 'xx') were used during simulations in all cases examined in this chapter.

The experimental results differ from the simulated ones to some extent as the actual material parameters may differ to some degree from their ideal values due to fabrication defects. Also, some geometrical parameters vary from one column of antidots to another. On the other hand, while using the PBC all column are assumed to be identical. Further,

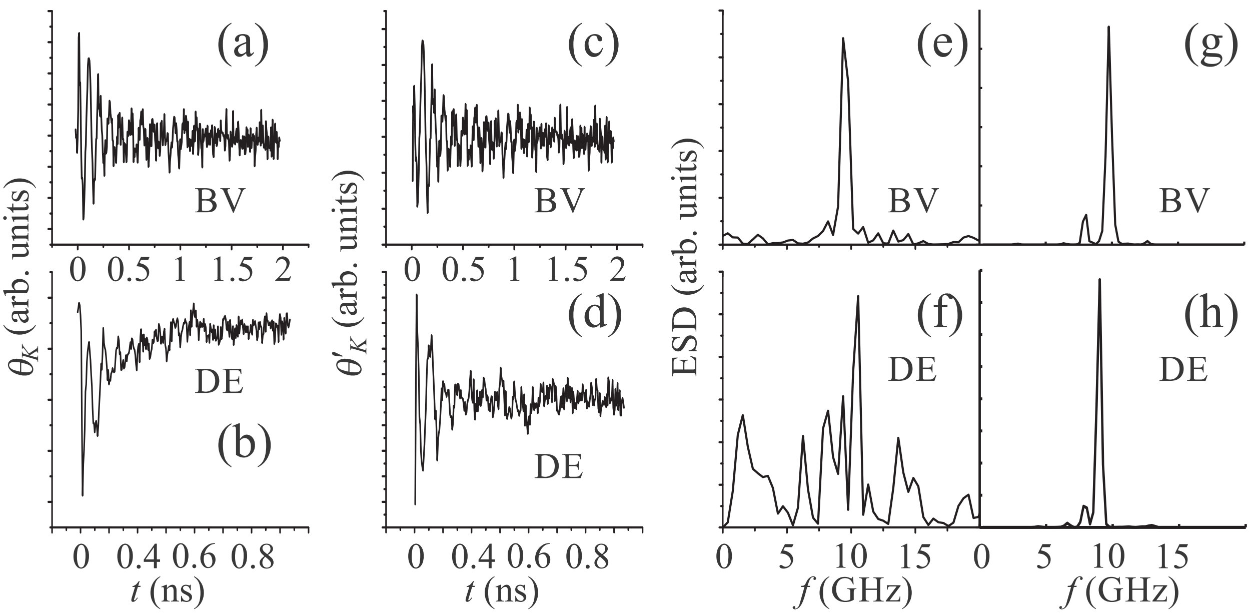

Figure 11.4.: TR–MOKE and simulation data for ① in (top row) BV and (bottom row) DE configurations. (a) and (b) show the time resolved Kerr rotation (θ_K) signal on a linear scale as obtained during experimentation. (c) and (d) represent the same signals with their bi–exponential backgrounds subtracted (θ'_K). (c) and (g) show the corresponding ESDs. ESDs are also calculated using micromagnetic simulations for (d) BV and (h) DE configurations. Bias field strength is 1 kOe in all cases.

the simulations are performed at an absolute zero temperature. Also, the use of PBC causes a reduction in observed number of modes.[303] PBC is used nonetheless, because simulation of the entire geometry would otherwise require forbiddingly vast computational resources. Thus, we generally expect a mode which is observed in simulation to be present in the experimental measurements, but not vice–versa. However, in few simulation results, artificial periodicity may produce a spurious mode or cause a mode to shift along the frequency axis. Henceforth, we represent the set of peaks observed during a simulation by $\{f_S\} : f_S \in \{f_S\}$. The set of experimentally observed peaks $\{f_E\}$ can then be constructed such that the sum $\sum (f_E - f_S)^2$ is minimized.

For a deeper understanding of the origin of SW band structure, one needs to consider the power and phase distribution of SWs as a function of position.[4,49,50,64,65,68,117,262,324–326] The same has been tabulated in Fig. 11.5 for different cases. The first and the third columns mark the case by declaring the sample ID, the peak frequency f_S, the magnetic bias field strength H_{bias} and the configuration (BV or DE). The second and the fifth columns depict the power profiles and the third and the fourth columns depict the phase profiles. Six columns of holes are shown in each case by placing the simulated geometry nine times side–by–side (1D PBC has been used along the length of the waveguide).

In the simulated geometry, the presence of antidots divides the waveguide into two sub–waveguides. However, in reality this division is not complete as the rows of antidots are shorter than the waveguide itself. For the BV configuration corresponding to Fig. 11.4 (g), we have $\{f_S\} = \{8.06, 9.77, 12.70\}$ GHz and $\{f_E\} = \{8.20, 9.38, 10.94\}$ GHz. As seen in Fig. 11.5, the first two modes correspond to BV mode (located amidst the antidot lattice) and the ferromagnetic resonance mode (of the two sub–waveguides), respectively. The third mode is a highly quantized mode resonating in the antidot lattice itself. Since, during fabrication, the distance between any two column of antidots, a_x, can vary by $\pm 10\%$,[64] we can see a number of modes around this region in Fig. 11.4 (e). For the DE configuration corresponding to Fig. 11.4 (h), we have $\{f_S\} = \{6.59, 7.81, 9.03\}$ GHz and $\{f_E\} = \{6.25, 8.20, 9.38\}$ GHz. As the bias field points along the width of the waveguide, demagnetized regions develop near the edges. Thus, the first mode here corresponds to the edge mode which is also confirmed by Fig. 11.5. The second mode is the DE mode, which corresponds to the demagnetized regions in the antidot lattice itself. Apart from the antidot lattice, this mode also resonates some distance away from the edges of the waveguide. Most of the power of the third mode is present in the two sub–waveguides. Another mode seen above 12.5 GHz possibly results due to highly quantized SW resonance as seen in the BV configuration as well. As the use of 1D PBC creates a stronger partition between the two sub–waveguides the resulting demagnetization becomes more pronounced leading to an overall negative shift in the SW frequency domain.

11.3.2. Dependence of SW Spectrum on the Lattice Parameters

The dependence of SW spectrum on the lattice parameters of the arrays (as given in Tab. 11.1) is shown in Fig. 11.6. The observed peaks have been analysed qualitatively to understand their nature. These peaks are also tabulated in Tab. 11.2 for a quantitative comparison. As the peaks move with changes in the lattice constants, a clear tunability transpires. Their power and phase distribution has also been presented in Fig. 11.5. A high

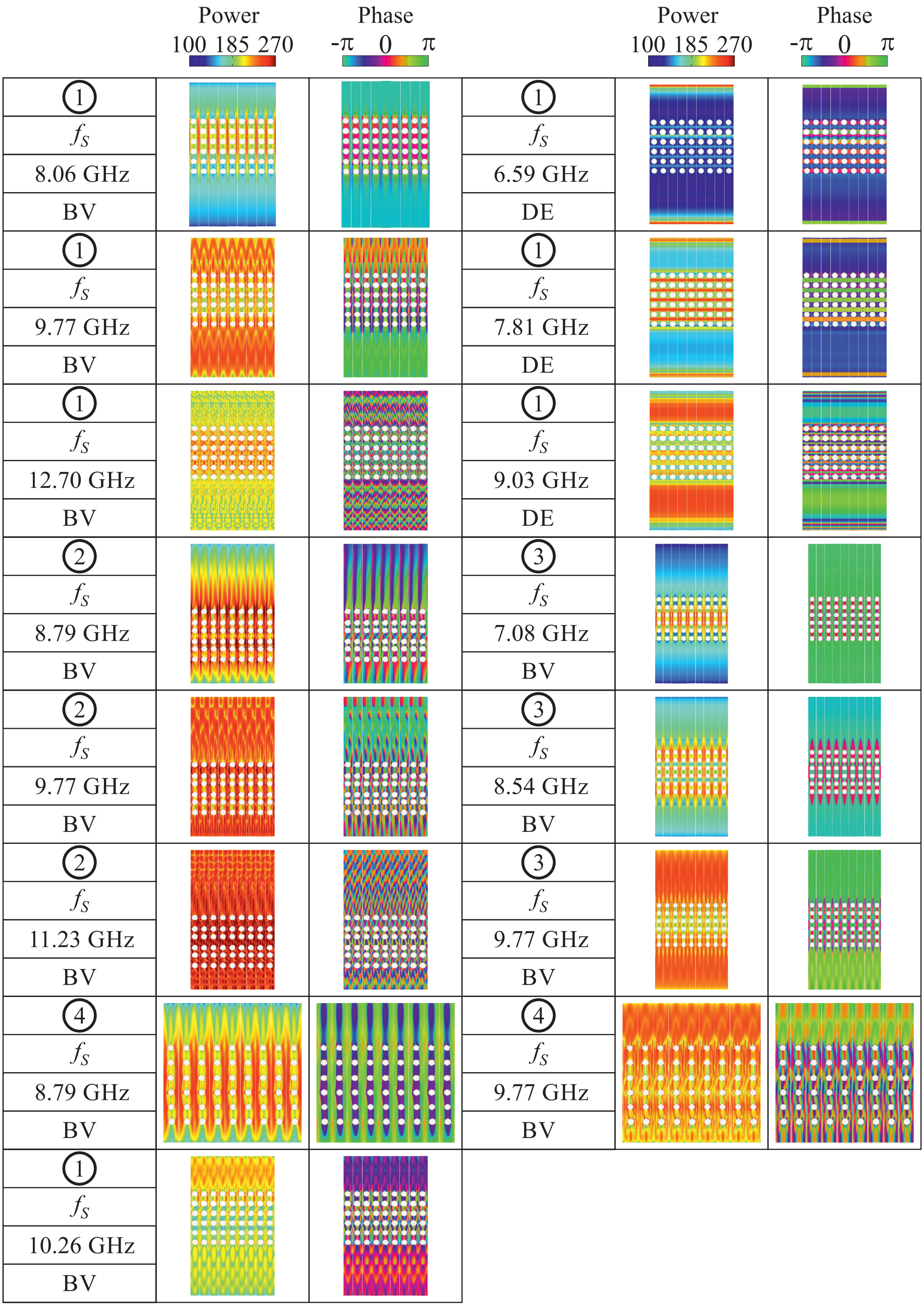

Figure 11.5.: SW power and phase calculated for different cases as marked in the first and the third columns. Bias magnetic field strength is at 1 kOe in all cases.

amplitude peaks is observed in all simulated cases at $f_S = 9.77$ GHz. This corresponds to the ferromagnetic resonance in the sub–waveguides (see Fig. 11.5). As the sub–waveguides occupy a vast area, a peak of high amplitude can be expected. As $a_{y1} + a_{y2}$ is the highest for ④, the area of sub–waveguides is minimized, resulting in a peak with lower amplitude. Thus we note that the average relative SW power of different modes can be controlled by changing the areas of the regions that they occupy. Depending upon the position of the array of antidots, the width of the sub–waveguides may be different. As seen in Fig. 11.5, this can lead to a small phase difference ($\ll \pi$) between the sub–waveguides in a few cases.

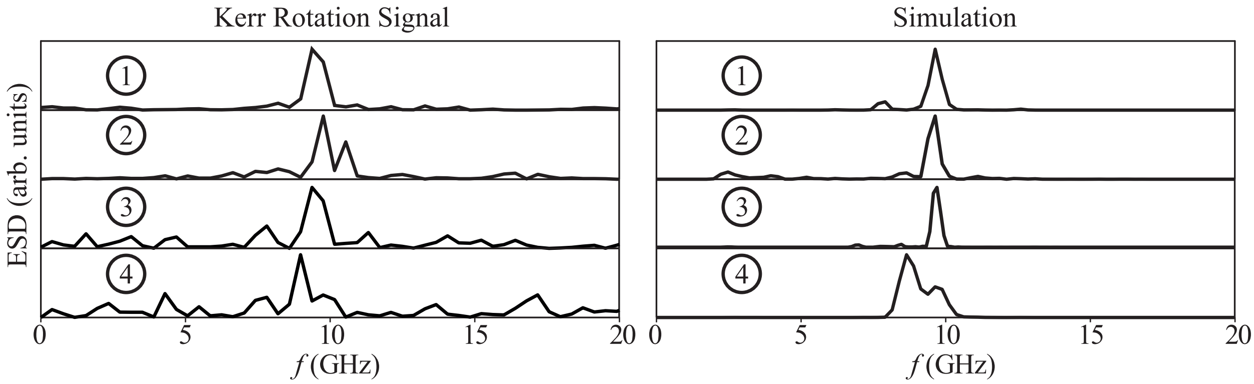

Figure 11.6.: SW ESD calculated using (left column) Kerr signal and (right column) simulations for ①, ②, ③ and ④ with a constant bias magnetic field strength $H_{\text{bias}} = 1$ kOe along the length of the waveguide. A linear scale is being used to represent the peaks here.

Table 11.2.: $\{f_S\}$ and $\{f_E\}$ for results presented in Fig. 11.6.

Sample ID	$\{f_S\}$ **(GHz)**	$\{f_E\}$ **(GHz)**
①	$\{8.06, 9.77, 12.70\}$	$\{8.20, 9.38, 10.94\}$
②	$\{8.79, 9.77, 11.23\}$	$\{8.20, 9.77, 10.55\}$
③	$\{7.08, 8.54, 9.77\}$	$\{6.64, 7.81, 9.38\}$
④	$\{8.79, 9.77\}$	$\{8.98, 9.77\}$

The peaks attributed to the ferromagnetic resonance of the sub–waveguides appear to agree well with corresponding experimentally observed peaks. In all cases at least one BV mode, localized amidst the antidot array, is observed between 8 GHz and 8.8 GHz with little or no quantization. For ③ another BV mode is seen at 7.08 GHz. For ② as well, multiple BV modes are seen below 5 GHz, with relatively lower quantization (these modes are not shown in Fig. 11.5). As these modes are localized in the antidot lattice, their position (in the frequency domain) is more sensitive to fabrication related fluctuations of lattice parameters d, a_x, a_{y1} and a_{y2}. Quantized modes in the antidot lattice is also seen for ① and ② above 10 GHz. When compared with the experimental results, these modes show more movement possibly because the quantization increases the sensitivity towards any variance in the lattice structure. These observations suggest that modes localized amidst the antidot array may be more sensitive to the precision of the fabrication processes.

11.3.3. Bias Field Dependence

We noticed that the peak associated with the ferromagnetic resonance of the sub–waveguides did not vary significantly with lattice constant in Fig. 11.6. This peak largely depends upon the magnitude of the applied bias field. In Fig. 11.7, we show the field dependence of SW band structure for a uniform waveguide and ① and ③. Bias field strengths of 1 kOe (maximum), 821 Oe, 692 Oe, 587 Oe and 492 Oe (minimum) were used for this experiment. A low frequency peak is visible in some experimental measurements. Typically it is associated with normal low frequency noise which occurs during TR–MOKE measurement and is filtered out during post processing by using a high pass filter. However, here the peaks, which appear systematically for certain bias magnetic field magnitudes — 821 Oe in all cases and 692 Oe for ③, have been presented as it is to allow for the readers to develop their interpretation independently.

A single peak which decreases monotonously with decreasing H_{bias} is seen in the case of the uniform waveguide. Experimentally observed peaks also appear to (qualitatively) agree with this Kittel mode (see sub–Sec. 2.3.3). This also helps to confirm that magnetic material parameters for simulations have been well chosen and the bias field values are well calibrated. Let us recall the Kittel formula (Eq. (2.52)):

$$\omega = |\bar{\gamma}| \sqrt{\left(H_{\mathrm{bias}} + \left(N_{yy} - N_{xx}\right) M_{\mathrm{s}}\right)\left(H_{\mathrm{bias}} + \left(N_{zz} - N_{xx}\right) M_{\mathrm{s}}\right)},$$

where the bias field points along the $x-$ axis for the wide waveguides considered here. Thus, we can also assume $N_{xx} \approx 0$ and $N_{zz} \approx 1$ (normal to the plane of the waveguides). Hence,

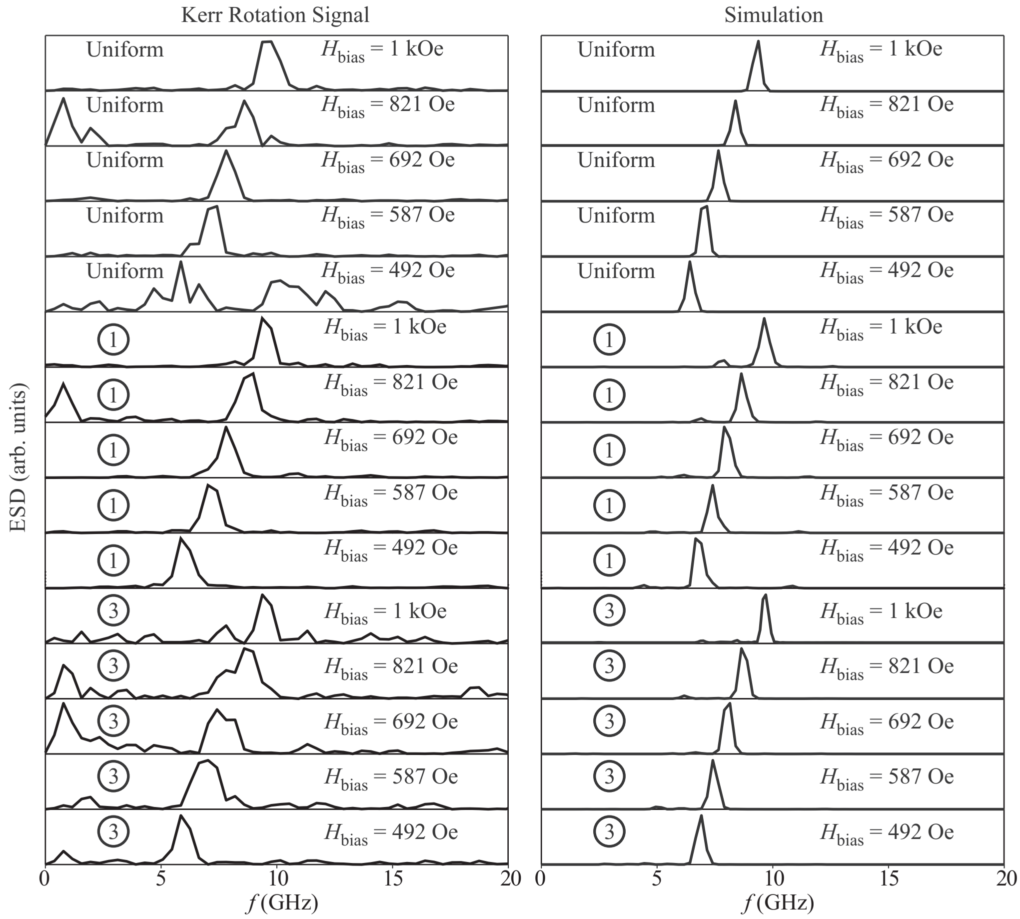

Figure 11.7.: SW spectra calculated using (left panel) Kerr signal and (right panel) simulations for a uniform waveguide and samples ① and ② with varying bias magnetic field strength H_{bias} along the length of the waveguide.

the Kittel formula reduces to:[49]

$$\omega = |\bar{\gamma}| \sqrt{(H_{\text{bias}} + N_{yy} M_{\text{s}}) (H_{\text{bias}} + N_{zz} M_{\text{s}})}. \tag{11.3}$$

Substituting $N_{zz} = 1 - N_{yy}$ (see Eq. (2.49)) in the above equation, we get

$$\omega = |\bar{\gamma}| \sqrt{(H_{\text{bias}} + N_{yy} M_{\text{s}}) (H_{\text{bias}} + (1 - N_{yy}) M_{\text{s}})}. \tag{11.4}$$

While using Eq. (11.4) to fit the simulated results, we get N_{yy} as 0.004378, 0.009288 and 0.01148 for uniform waveguide, ① and ③, respectively. Thus, we note that the presence of the antidot array close to the centre of a uniform waveguide can nearly double the demagnetizing factor N_{yy} — which can be further tuned by changing the lattice parameters (from ① to ③). The plots of Eq. (11.4) corresponding to the aforementioned values of N_{yy} are shown in Fig. 11.8. Experimentally observed modes in different cases are represented by open symbols. For decreasing bias field strength, the modes in patterned waveguides (① and ③) appear to drop more rapidly than predicted. This may be the result of a change in the equilibrium magnetic configuration leading towards a more non-uniform magnetic state and a reduced effective magnetic field and precession frequency.

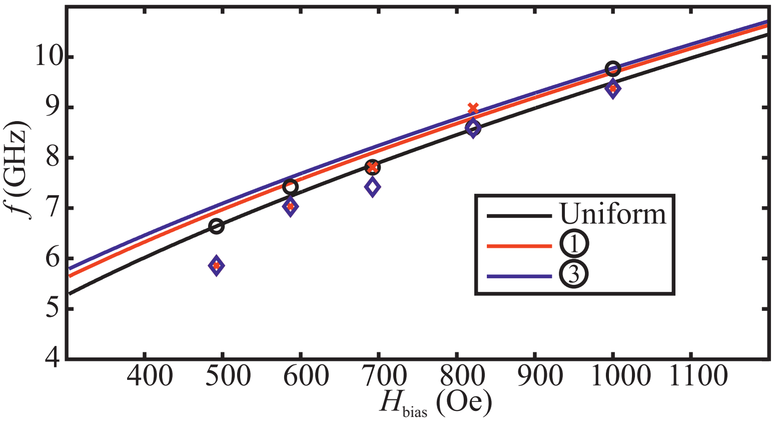

Figure 11.8.: (Solid lines) Curve fitting of simulated modes (shown in Fig. 11.7) using the Kittel formula (Eq. (11.4)). (Open symbols) Experimentally observed modes.

It can be noted that the experimentally observed peaks in Fig. 11.7 are always wider than the those seen in simulation. This can be corrected by using a higher Gilbert damping constant. However, doing so will compromise the resolution of simulated results. ④ is visibly asymmetrical (see Fig. 11.5). We know from Chap. 6[4] that the wider and the narrower sub–waveguides should resonate at different frequencies. However, here the difference is merely of about 0.5 GHz and the currently used Gilbert damping constant of 0.008 does not allow to resolve this phenomena. Also, since the wider sub–waveguide occupies a greater area, its peak is seen more prominently due to averaging. The evidence of this undetected splitting can be noticed by comparing the power and phase profiles at 9.77 GHz and 10.25 GHz in Fig. 11.5 for ① ($H_{\text{bias}} = 1$ kOe). The peak seen in Fig. 11.7 for ① ($H_{\text{bias}} = 1$ kOe) is at 9.77 GHz. In Fig. 11.5, this peak is seen to have greater power in the wider sub–waveguide. The narrower sub–waveguide shows more power at 10.25 GHz. This splitting is not resolvable in the experimental results as well probably due to the presence of an even higher damping.

From Fig. 11.5, we can see that the three modes which are evident at all bias field strengths

H_{bias}, shift negatively along the frequency scale with reducing H_{bias}. The lowest and the highest modes are the BV and the quantized modes (with power distribution close to the antidot lattice) in all cases. The mode in the middle corresponds to the ferromagnetic resonance of the two sub–waveguides. As mentioned earlier, the two sub–waveguides resonate at slightly different frequencies, where that difference is lower than the mode width observed here. As seen in Fig. 11.5, ③ features two BV modes (with limited quantization) with power close to the antidot array for all cases except $H_{\text{bias}} = 821$ Oe. As in the case of ①, the most powerful mode for ③ (as seen from Fig. 11.7), is again situated in the space of the two sub–waveguides. The entire band structure shifts negatively for ③ with decreasing values of H_{bias}.

11.4. Conclusions

In this chapter, we were able to demonstrate the tunability of magnonic spectra of MAWs based on their geometrical parameters and the bias magnetic field. All discussion here was limited to modes seen at the centre of the Brillouin zone. We showed that SW modes in the sub–waveguides were very stable towards any variance in the fabrication parameters. They were largely controlled by the orientation and magnitude of the bias magnetic field $\mathbf{H}_{\text{bias}}$. Edge mode of the MAW was clearly observed in the DE configuration. No edge mode was observed in the BV configuration due to the inherent shape anisotropy of the waveguide. Modes with power close to antidot lattice showed a greater dependence on the geometrical parameters as minor disagreement between simulation and experimental results was observed here. Quantized modes were also seen to have power close to the antidot lattice. The experimentally observed modes here showed greater disagreement hinting at higher sensitivity towards changes in the geometrical parameters from one column of antidots to another. We can thus conclude that some advances in the fabrication procedures relating to reducing variance in geometrical parameters of the fabricated samples need to happen in order to readily create reliable SW waveguides or filters. Alternatively, computational methods may be improved upon so that samples which can be fabricated readily are simulated in a reasonable amount of time.

12. Coupled Magnetic Vortices for All–Magnetic Transistor Operations

*There has been a revolution in the study of inhomogeneous and non-trivial magnetic nano–structures such as magnetic vortices and antivortices due to their suggested applications in magnetic data storage, magnetic random access memory,[128–131] magnetic logic[132] and information processing devices.[132]

In our study we show that off–resonant signals[327] of lower amplitude can be used to design suitable transducers with isolated vortices, which will be required to convert other kinds of external signals (*e.g.* a rotating field) to vortex core gyration. In the case of a pair of magnetostatically coupled vortices, if a signal is applied to only of them then the other one shows a greater core gyration i.e., amplification when the core polarities are opposite. Antivortex solitons moving through the stray field are held responsible for this behaviour. We postulate some rules regarding their dynamics and use them to mimic transistor–like operations of switching and amplification with a chain of three vortices. Furthermore, we attempt to couple the output of this three vortex chain to two symmetrically placed daughter chains in an attempt to demonstrate a fan–out operation. However, the antivortices involved in the dynamics favoured one branch over the other resulting in a higher level of asymmetry – one of the branches received more power than the other.

*This chapter is based upon Kumar *et al.* *Sci. Rep.* **4**, 4108 (2014).

12.1. Methods

Magnetic vortex dynamics was simulated using the finite difference method based Landau-Lifshitz-Gilbert (LLG) ordinary differential equation solver called Object Oriented Micromagnetic Framework (OOMMF). Before the dynamics could be observed, a magnetic ground state has to be achieved with required vortex core polarity and chirality.[128,129,148,230,328–332] This was accomplished by using a pulse field $H_t = H_0 \exp(-t'^2)$. Here, $\mu_0 H_0 = 1$ T and normalized time $t' = (t - t_0)/(\sqrt{2}\sigma)$. $t_0 = 75$ ps and σ is the standard deviation of this Gaussian pulse in time whose full width at half maximum is 30 ps. Close to the centre of the circular geometries we apply $H_z = \pm H_t/10$ along the Z axis where the sign controls the core's polarity. If the origin of co-ordinates is brought to the centre of the vortex then $X-$ and $Y-$components of fields, H_x and H_y that would produce the desired chirality are given below

$$H_x = \mp H_t \sin(\theta);$$
$$H_y = \pm H_t \cos(\theta).$$

Here, $\theta = \tan^{-1}(y/x)$ and the upper or lower signs were chosen for CCW or CW chiralities, respectively. It is to be noted that this pulse signal controlled by H_t, dies down quickly while the magnetic ground state is obtained by running the simulation for 40 ns under a high damping (Gilbert damping constant $\alpha = 0.95$ is used in the LLG equation). We have used saturation magnetization, $M_s = 0.8\times10^6$ A/m, exchange constant, $A = 13\times10^{-12}$ J/m and zero magneto–crystalline anisotropy. During vortex dynamics simulations we reduce α to a more realistic value of 0.008 for Py. Magnetization was observed every 10 ps for about 40 ns during dynamics. The cell size used during simulation was 5 nm $\times$ 5 nm $\times$ 40 nm.

Before we start to explore the dynamics of magnetic vortices, we first need to obtain the natural frequencies associated with a single isolated vortex. A broadband excitation signal was given to reveal these frequencies. The signal had only X-component, H_x^S which contained power up to $f_{\mathrm{cut}} = 45$ GHz and depended upon time t as given by:

$$H_x^S = H_x^0 \frac{\sin(2\pi f_{\mathrm{cut}}(t - t_0))}{2\pi f_{\mathrm{cut}}(t - t_0)}.$$

Here, $\mu_0 H_x^0 = 0.05$ T and $t_0 = 200$ ps.

Upon obtaining the magnetization data from OOMMF, we chose to analyse the results by looking at the time evolution of spatial average of normalized $X-$component of magnetization, $\langle m_x \rangle$ for each vortex, and its corresponding ESD. Normalization is done by dividing the $X-$component of magnetization, M_x by M_s; such that $m_x = M_x/M_s$. The Hanning window is used on $\langle m_x \rangle$ to reduce spectral leakage. The windowed data is then zero padded and Fourier transformed to obtain the required ESD, $|\bar{m}_x|^2$.[262] This is plotted in figures on decibel scale as $w_H \times 20 \log_{10} |\bar{m}_x|$, where a window scaling factor of $w_H = 2$ is used for the Hanning window. These ESDs were calculated after running the dynamics for over 40 ns, so that any transient vortex core dynamics are suppressed and steady state dynamic solutions appear to be more prominent in the spectrum. Power spectral density is considered to be more desirable in the case of persistent signals. However, here we run the simulations for finite amount of time. Also, natural damping ensures that net power input to the system becomes zero before the simulations finish. The stray field is also obtained from OOMMF during dynamics. The stray field plots were created using MATLAB. The contour colouring is based on the sum of squares of $X-$ and $Y-$components of the stray field.

12.2. Results and Discussion

We use permalloy (Py: $Ni_{80}Fe_{20}$) with negligible magneto–crystalline anisotropy in the form of a 40 nm thin disk of diameter $2R = 200$ nm to ensure a stable vortex structure.[258] The darker shade in Fig. 12.1 (a) represents such an isolated vortex. Figure 12.1 (b) shows a pair of coupled vortices whose centre to centre distance is $a = 250$ nm. A chain of three vortices, with the same centre to centre distance a, has also been studied with different orientations of polarity. Spatially averaged $X-$component of magnetization $\langle m_x \rangle$ has been used as an indicator of core displacement away from their equilibrium positions. The square of the amplitude of Fourier transform of $\langle m_x \rangle (t)$ (with respect to t) – also known as the energy spectral density (ESD) – shows the peaks in vortex core dynamics as a function of frequency.

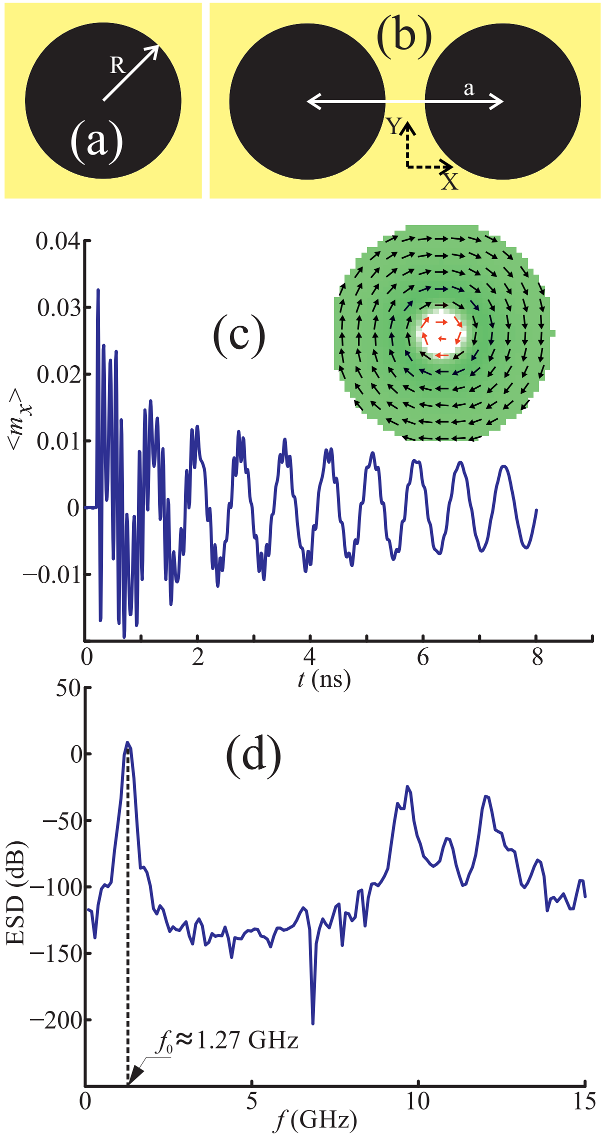

Figure 12.1.: Dark regions represent the 40 nm thick (a) isolated and (b) coupled pair of magnetic vortices each of diameter $2R = 200$ nm. The centre to centre separation in the case of coupled vortices is set to $a = 250$ nm. (c) Time evolution and (d) corresponding energy spectral density of $\langle m_x \rangle$ in response to the signal H_x^S.

12.2.1. Isolated Magnetic Vortex

Figure 12.1 (c) shows a plot of $\langle m_x \rangle$ vs. time and Fig. 12.1 (d) shows the associated ESD (in decibel) for the single vortex excited by a broadband signal. The gyrotropic mode is observed at frequency $f = f_0 \approx 1.27$ GHz. Higher frequency modes associated with the generation of spin-waves[333] are also observed. Here, we concern ourselves with frequencies $f \leq f_0$ while using signals that are rotating CW or CCW in the plane of the magnetic vortices. With up polarity $p = 1$, CCW signals are known to produce greater gyration[152] which can lead to polarity switching. This can be useful in terms of data storage.[327] However, if the polarity switching is somehow avoided, one can use this to create a suitable transducer for appropriately rotating signals. To that end we can use signals with lower amplitude. Signals with off–resonant frequency $f < f_0$, should be used to reduce the convergence time. As shown in the Fig. A.1, anharmonicity of the gyration dynamics results in a beating frequency when off–resonant signals are used. A trade–off between convergence time and beating frequency needs to be further explored as a design consideration.

12.2.2. Coupled Magnetic Vortices Pair

We have examined the transfer of energy from one vortex to another in terms of their core gyration amplitude (measured in terms of $\langle m_x \rangle$) when excitation is only given to one of them. Here, $\langle m_x \rangle$ is computed for both the vortices separately. The dynamics was examined with all sixteen combinations of polarity and chirality of the two vortices. When a small external bias field is applied, the vortex cores may move up or down along the $Y-$axis. This changes their separation and causes magnetic surface charges to appear on the vortex boundaries; consequently affecting the strength of their magnetostatic coupling.[9,137] Hence, in the presence of a bias field, if both the vortices have the same chirality, their coupling will remain relatively unaffected, than when they have different chiralities. This phenomena can be used to affect a chirality dependent dynamics and signal transmission. However, in the absence of an external bias, we observed that chirality does not play any role towards enhancing the asymmetry in dynamics, as described below. Thus, henceforth all vortices in this work have CCW chirality. Furthermore, observable changes only appeared to occur between cases with similar and opposite polarities.[156] Mediated by several factors,[150,334–337] the resonant frequencies of a pair of vortices can differ from that of an isolated vortex. However, in this study, we used an excitation signal rotating at frequency f_0, which is applied only on the left disk (Fig. 12.1 (b)). Figures. 12.2 (a) and (c) show the results for the case when both polarities are up ($p_1 p_2 = 1$) and Figs. 12.2 (b) and (d) show those when left core is up and right core is down ($p_1 p_2 = -1$). Figures 12.2 (a) and (b) correspond to a signal amplitude of 0.5 mT and Figs. 12.2 (c) and (d) correspond to a signal amplitude of

1.5 mT. To ascertain that the results discussed here are independent of cell size, Fig. 12.2 was reproduced using a cell size of 2.5 nm × 2.5 nm × 40 nm. The same has been shared as Fig. A.2. Although the form of the peaks have changed to some extent, the relative gains at $f = f_0$ remain largely unaffected.

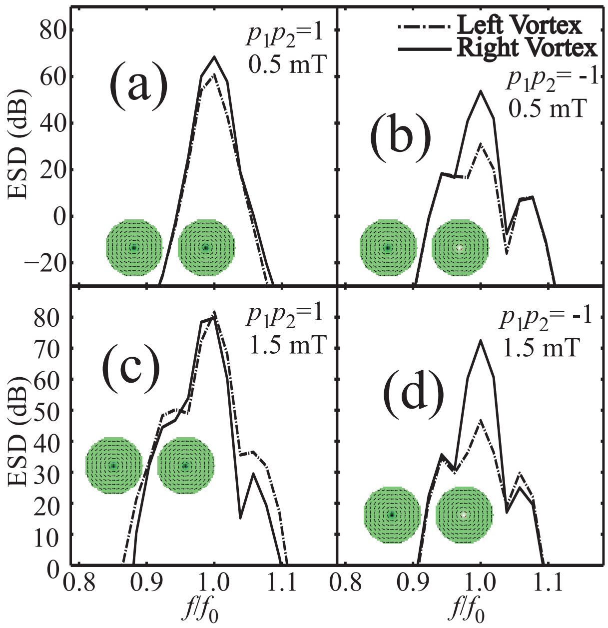

Figure 12.2.: ESDs of left and right magnetic vortices shown in the insets with ((a) and (c)) similar and ((b) and (d)) opposite polarities. (a) and (b) show the results for a signal amplitude of 0.5 mT while (c) and (d) show those for an amplitude of 1.5 mT, both rotating CCW at $f = f_0$.

With increase in the signal amplitude from 0.5 mT to 1.5 mT, we see a splitting[338] of the peak. Furthermore, when $p_1p_2 = -1$, more energy is transmitted and stored in the right vortex. For signal amplitude of 0.5 mT and $p_1p_2 = 1$, the left vortex, exhibits 60.72 dB of ESD at its gyrotropic mode while the right vortex exhibits 68.43 dB. While for $p_1p_2 = -1$, these values become 30.99 dB and 53.69 dB, respectively. Thus, the difference in ESDs of gyrotropic modes of left and right vortices increases by about 15 dB. When signal amplitude is increased to 1.5 mT, these values become 81.66 dB (left vortex) and 79.76 dB (right vortex) for $p_1p_2 = 1$ and 46.67 dB (left vortex) and 72.45 dB (right vortex) for $p_1p_2 = -1$. Here (for $p_1p_2 = -1$), the ESD (at $f = f_0$) of the right vortex is 25.78 dB greater than that of the left vortex. This shows that opposite core polarity facilitates amplification of signal transfer, which is further enhanced by the input signal amplitude. An increase in about 9.5

dB in signal power (from 0.5 mT to 1.5 mT) has caused the difference in gain to increase by 12.69 dB. The dependence of this relative amplification on the strength of the input signal is essential to mimic the transistor operation where the base current controls the amplification.

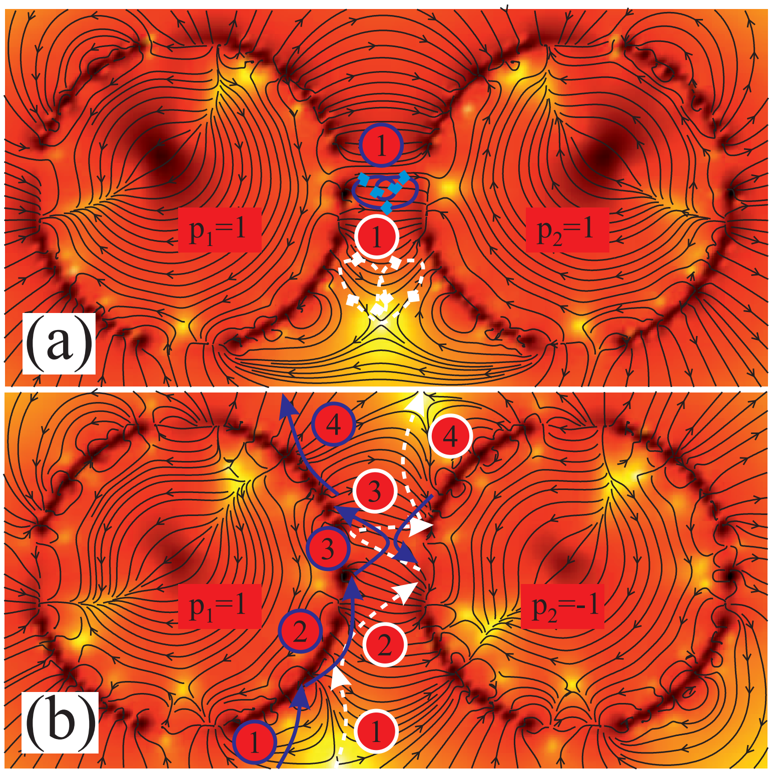

Figure 12.3.: Stray field distribution showing the path of travelling antivortex packets for $p_1p_2 = 1$ (a) and $p_1p_2 = -1$ (b). With time the packets shift their path from the dashed to the solid lines.

These observations, along with the ones made for an isolated vortex, testify to the existence of anharmonic and asymmetric dynamics present in the vortex core gyration, which cannot be explained by solutions of the Thiele's equation with linear approximations;[146,233,339] even if vortex core deformation[221] is taken into account. Although, the type of amplification described here has not been seen before, asymmetry based on polarity in terms of energy transfer rate and efficiency has been observed experimentally. Stronger or weaker stray field coupling can affect the rate of energy transmission,[155] but it does not guarantee the observed asymmetry in general and amplification in particular.

One may draw an analogy of this observation with a driven double pendulum made of identical pendulums. In this case, when the driving frequency is same as the eigenfrequency of the isolated pendulum then the top pendulum mass becomes stationary while the bottom pendulum mass moves with an amplitude twice as that of the driving amplitude. This may be considered as an infinite amplification (although, the angular displacement of the top pendulum will still not be zero). However, for a coupled pendulum, where two pendulums are connected with a spring and dynamics is not pinned at any end (this system is closer to the coupled vortices presented here in terms of underlying equations of dynamics), no such amplification occurs when the driving frequency is the same as the eigenfrequency of the individual pendulum[340] (see Sec. A.1). Either way, a direct comparison of the energy transfer mechanism of coupled magnetic vortices with that of coupled mechanical oscillators is difficult due to the presence of additional parameters in the former case. The gyrovector, which serves as the inertia of the vortex core[149] can switch direction with core polarity resulting in the amplification observed here. Hypothetically, this will be comparable to obtaining an amplification in one of the coupled pendulums by changing its inertia from I to $-I$. An analytical model is yet to be developed to describe this phenomenon; but, this is outside the scope of this work (see Sec. A.1). Here, we considered a numerical approach and calculated the temporal evolution of the stray field and discovered that packets of antivortex structures travelling through the stray field mediate the transfer of energy between the two vortices. The path of these antivortices are shown in Fig. 12.3 for both polarity combinations when the excitation signal amplitude is at 1.5 mT. As time progresses the path shifts from dashed to solid lines.

As seen from Fig. 12.3 (a), a single antivortex packet moves in a closed path for $p_1 p_2 = 1$. This packet collides with other antivortex structures which originate at the boundaries of the nanodisks. We understand that the antivortex packets discussed here are not particles in the true sense and their apparent 'collision' is only a result of the interacting stray fields. This interaction (or collision) is also shown in the Supplementary Movie M1*. It is only during this collision that these antivortex 'solitons' ('soliton' has been used loosely here to describe even those short–lived antivortex packets which do not possess consistent form for significant duration) are allowed to change their size (local field distribution) significantly.[341] When it collides with the left disk, which initially has more gyrotropic energy, it becomes smaller and when it collides with the right disk, it becomes larger. This indicates that there

*Movie M1: https://www.youtube.com/watch?v=RBLSFu8RHx0 is an inverse relation between the size of the antivortex and the gyrotropic energy that it can transfer. As time progresses and the amplitudes of the gyrating vortex cores become comparable, the path of this bouncing soliton becomes smaller and it moves to a location shown by the solid line ① in Fig. 12.3 (a). The soliton itself does not change greatly in size after this point indicating no significant transfer of energy.

Figure 12.3 (b) shows that more than one antivortex solitons are involved in the energy transfer for the case when $p_1 p_2 = -1$. On a given vortex boundary, as one soliton gets terminated, another one is created. This creates a cascade of solitons, which vary in size (see Supplementary Movie M2*). At first, the dashed lines mark the path of this cascade with the large arrowheads showing where a soliton gets localized. Branches are numbered from ① to ④, in an order such that the path of the new soliton is shown by the next branch. The path of this cascade changes gradually with time as well. Specifically, the number of rebounds between the boundaries of the vortices (the length of branch ③) may vary quite often. However, it is observed that as branch ① terminates, the remaining solitons, which follow branches ② and ③ are relatively smaller. When branch ③ terminates, a soliton of the same size as the first one (which traversed branch ①) emerges from the right vortex to trace the final branch ④. Thus the right vortex gains gyrotropic energy in the beginning of the dynamics. This cascade occurs twice every cycle, suggesting that signal transfer rate or efficiency can be controlled not only by the saturation magnetization[155] but also by the frequency of the signal and further optimization of signal transfer efficiency by tuning the dimensions of the coupled vortices is possible. As time progresses, the cascade starts to occur along the solid lines ① to ④, shown in Fig. 12.3 (b). When the gyration amplitude of the right vortex becomes a certain degree greater than that of the left one, we notice that the soliton, which was traversing the dashed branch ③ earlier, now starts from the boundary of the left vortex. However, it is deflected back by another soliton, which emerges from the right vortex – much like an electron or hole charge carrier being prohibited from crossing the depletion layer of a junction diode. We can turn this amplification 'on' or 'off' simply by switching the polarity p_2; but it may be technologically more desirable to have this control via a third vortex.

*Movie M2: https://www.youtube.com/watch?v=CKTtnawFYU4

12.2.3. Magnetic Vortex Transistor (MVT)

In order to examine this transistor–like behaviour, we now add another vortex towards the right of the vortex pair shown in Fig. 12.1 (b) to form a three vortex sequence with polarities (from left to right) p_1, p_2 and p_3, which take values of 1 or -1 denoting up or down polarities. In the previous sub-section, we identified relative polarity as the source of the observed amplification. Hence, here we study only the four cases with $p_1 = 1$ (up), $p_2 = \pm 1$ and $p_3 = \pm 1$. Chirality in all cases is CCW. Signal is applied to the left vortex only. The ESDs for these cases around frequency f_0 are shown in Fig. 12.4 (as shown in the insets, the excitation is given to shaded vortices only).

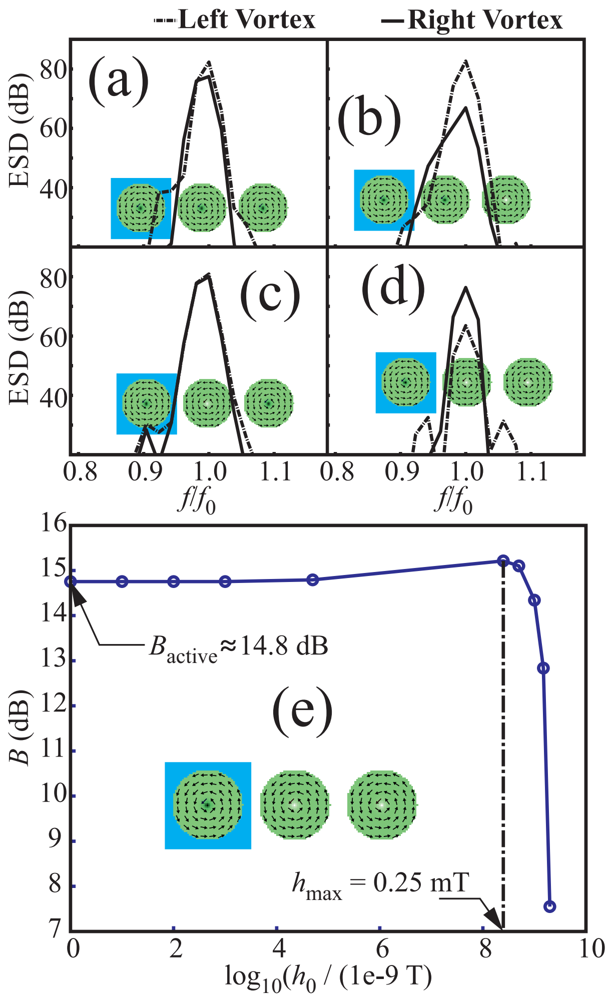

Figure 12.4.: ESDs of left and right magnetic vortices with (p_1, p_2, p_3) equalling (a) $(1, 1, 1)$, (b) $(1, 1, -1)$, (c) $(1, -1, 1)$ and (d) $(1, -1, -1)$ as shown in the respective insets. A 1.5 mT signal rotating CCW at frequency f_0 is applied only to the left (shaded) vortex. (e) Gain B, versus logarithm of signal amplitude h_0.

Splitting can be observed in a few cases in Fig. 12.4. Unlike the splitting seen with increase in signal amplitude (see Fig. 12.2 (c)), which happens due to inherent non–linearities of the dynamics,[338] here it occurs for a different reason: an increase in the number of vortices leading to an increase in the number of permutations of couplings in the system.[342] Below, we consider any difference in ESD at the signal driving frequency of $f = f_0$ only.

As seen in Figs. 12.4 (a) and (c), the transmission efficiency is equivalent for a persistent signal in both cases: $(1, 1, 1)$ and $(1, -1, 1)$; with the latter faring slightly better. Although, a third vortex was added in the chain, a gain of 12.84 dB (between right and left most vortices) is observed in Fig. 12.4 (d). Also, transistor like switching is observed clearly with the three vortex sequence considered here when changing from $p_2 = -1$ (high base current) (Fig. 12.4 (d)) to $p_2 = 1$ (low base current) (Fig. 12.4 (b)) changes the difference in signal levels of the right vortex (collector) from 12.84 dB to -15.71 dB. We define the gain B in Eq. (12.1) as below:

$$B \equiv \mathrm{ESD}_3(f_0) - \mathrm{ESD}_1(f_0). \tag{12.1}$$

Here $\mathrm{ESD}_1(f_0)$ and $\mathrm{ESD}_3(f_0)$ are ESD at $f = f_0$ for left and right vortices, respectively.

We further checked if this gain B, also depended upon the input signal amplitude h_0. Figure 12.4 (e) shows a plot of B versus h_0 for $h_0 =$ (1e-6, 1e-5, 1e-4, 1e-3, 5e-4, 0.25, 0.5, 1, 1.5, 2) mT. Left vortex's core reversed for $h_0 = 3$ mT; and hence, we limit ourselves to 2 mT. For lower values of h_0, the gain appears to be constant at $B = B_{\mathrm{active}} \approx 14.8$ dB. This is reminiscent of a bipolar junction transistor (BJT) operating under small–signal conditions.[343] At higher signal strength, the gain B, no longer remains constant. This indicates that like other electronic transistors, our 'magnetic vortex transistor' is also susceptible to non–linear distortion. The maximum value of gain $B = B_{\max} \approx 15.21$ dB is seen for a signal strength of $h_0 = h_{\max} = 0.25$ mT.

We further investigate the roles of the stray field antivortex solitons on the transistor–like operations described above. We begin by analysing the temporal evolution of the stray field for cases where (p_1, p_2, p_3) equals $(1, -1, 1)$ and $(1, -1, -1)$. The same is shown in

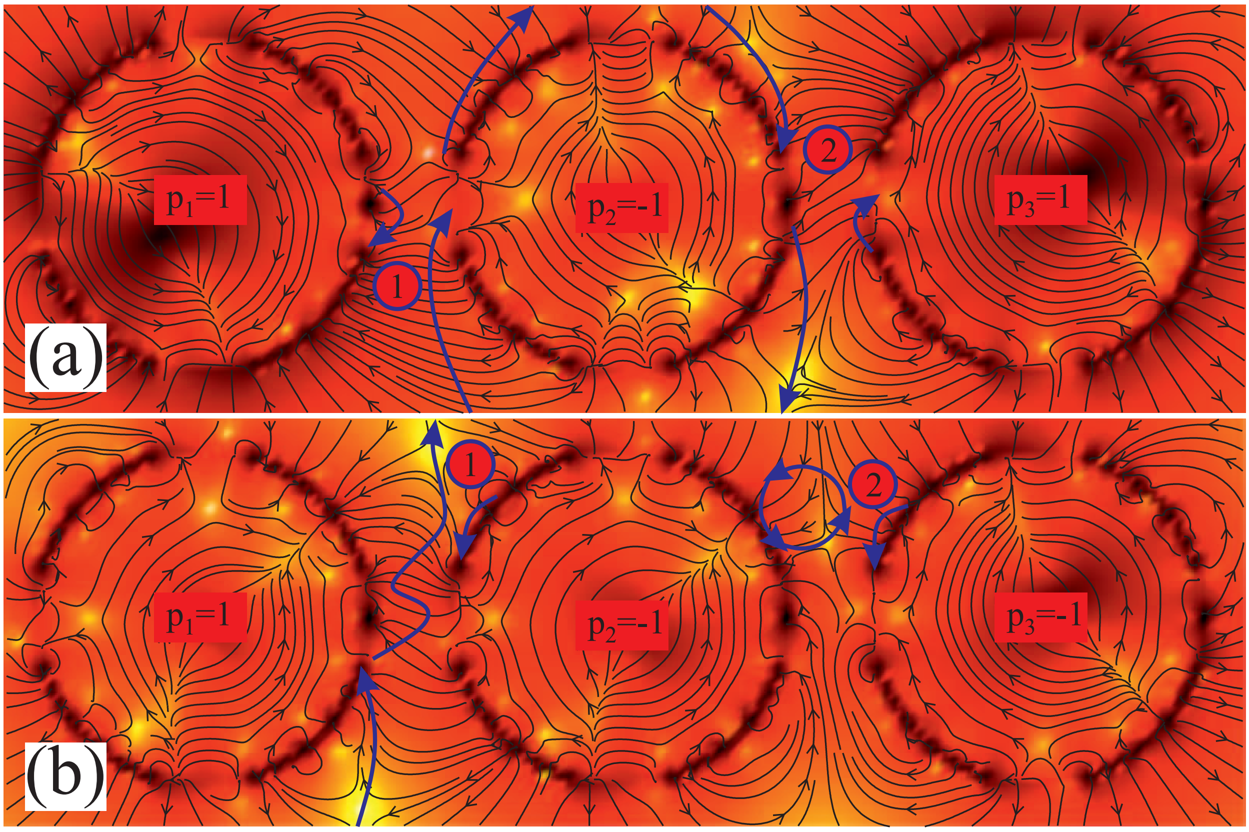

Figure 12.5.: Stray field distribution in the cases where (p_1, p_2, p_3) equals (a) $(1, -1, 1)$ and (b) $(1, -1, -1)$. The path of antivortex packets after the dynamics has stabilized is marked with solid lines.

Supplementary Movies M3* and M4†, respectively. Figures 12.5 (a) and (b) summarize the path of the solitons involved. Polarity dependent transient gyrotropic energy transfer between any two neighbouring vortices here too occur in the same manner as shown by the dashed lines in Fig. 12.3. These lines are omitted in Fig. 12.5 for clarity. Solid lines show the approximate paths the solitons follow after the dynamics had become relatively stabilized. For $(p_1, p_2, p_3) = (1, -1, 1)$, where no amplification ($B < 0$ dB) is observed, the cascade of solitons form a large oval loop around the central vortex. Energy appears to be transferred during collisions at ① and ②. This creates a closed feedback loop directly between the left and the right vortices. The solitons skip along the boundary of the central vortex on several occasions in order to aid their own cascade. Most importantly, we note here as well that solitons in the bottom half of the loop (right to left vortex) appear larger (lesser energy)

*Movie M3: https://www.youtube.com/watch?v=PdfHQesec9k
†Movie M4: https://www.youtube.com/watch?v=b-cr5752DwE

than those traversing the top half (left to right vortex). Thus the flow of energy still occurs from the left vortex, which is excited externally to the right one. However, an amplification ($B > 0$ dB) is observed for $(p_1, p_2, p_3) = (1, -1, -1)$ and Fig. 12.5 (b) sheds some light on this crucial finding. Here, the path of antivortex solitons between the left and the central vortex does not change greatly from its early transient stage. Here too, energy is transferred at the sites ① and ②, essentially from the left vortex to the right one. However, unlike in Fig. 12.5 (a), no feedback loop, and thus no energy rebalancing is present here. This leads to a unidirectional flow of energy as determined by the cascade of antivortex solitons. The right vortex core, thus builds up gyrotropic energy until its drag (or dissipation) matches the power influx. Thus an amplification of the gyrotropic mode of the right vortex is observed in this case. One can simplify the dynamics for the two cases analysed above by considering the central vortex as an efficient medium and taking it out of the picture. Then we can see that amplification was observed when $p_1 p_3 = -1$. However this amplification can be controlled by switching the polarity of the middle vortex (p_2), similar to what is done by switching the base current in a BJT.

12.2.4. Fan–Out

In an attempt to demonstrate a fan–out operation, which may support the development of more complex circuits, we placed two more MVTs symmetrically above and below the original MVT as shown in Fig. 12.6. Same material and structural parameters as before were used here. Power was given only to the left vortex of the original MVT. To our surprise, amplification was seen in only one of the branches. As in the inset of Fig. 12.6, the right vortex of upper branch in this network received about 15 dB more power than the lower branch. When all the core polarities in this network were reversed, the lower branch received the greater power by the same amount.

The cause of this asymmetry is the fact that the solitons do not split during a fan–out. Also, the antivortex seen between the first two vortices in Fig. 12.5 (b) goes on directly to hit the upper chain as marked in Fig. 12.6. Thus, further study regarding the implementation of a fan–out is warranted by looking at the path of these antivortices in different network configurations.

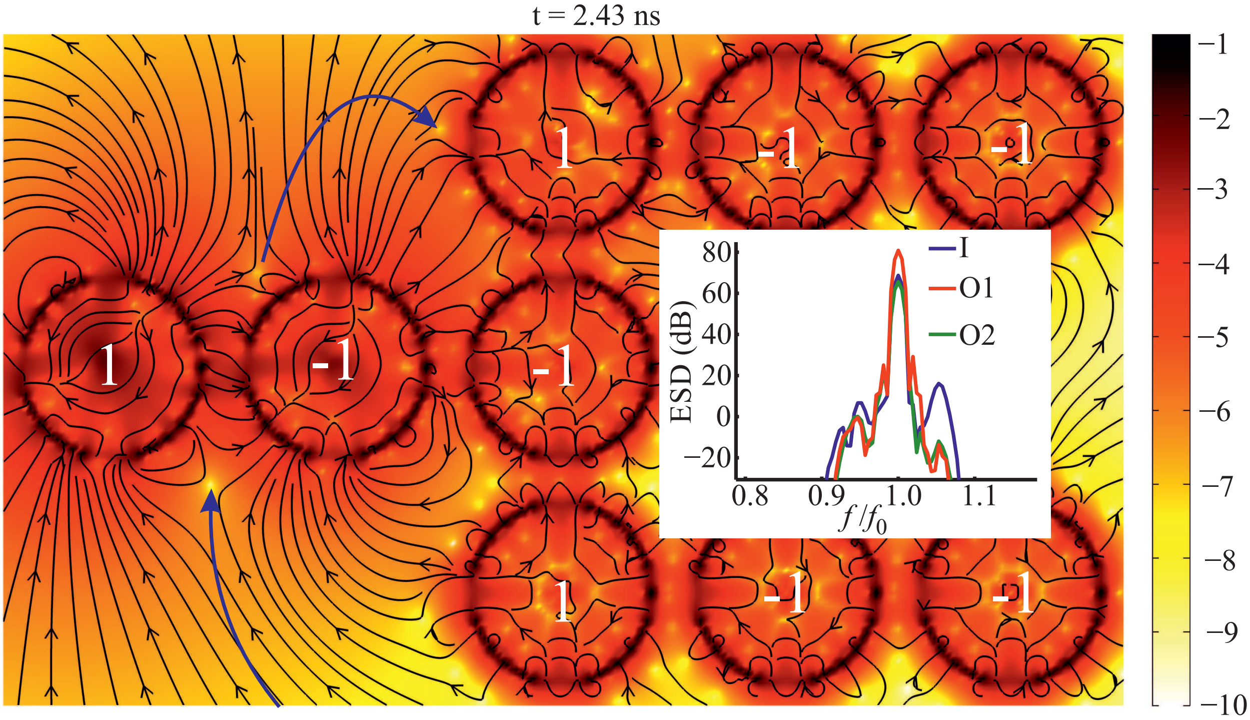

Figure 12.6.: Stray field distribution in a MVT network. Signal is given only to the left vortex in the middle row. Vortices are marked with their respective polarities. A path followed by antivortex packets taking energy from the left vortex in the middle chain to the left vortex of the top chain is marked. The ESDs of left and upper and lower rightmost vortices are given in the inset marked as 'I', 'O1' and 'O2' respectively.

12.3. Conclusions

We numerically examined the polarity dependent asymmetry and non–linearities in vortex dynamics. Cases presented in this chapter included isolated vortices and coupled two and three vortex sequences. We particularly examined the dynamics for gain in the transfer of gyrotropic mode power from one vortex to another. To start with, we describe the design considerations in creating a transducer which can convert power from an external rotating magnetic field signal to gyrotropic power. Best results were observed when the driving signal frequency was very slightly off–resonant w.r.t. the eigenfrequency of the transducer. In the case of coupled pair of vortices, when an excitation signal is applied to only one of the vortices then in certain situations, considerably more energy (a maximum gain of 27.68 dB) is transferred and stored in its neighbouring vortex if it has the opposite polarity. We further observed that this amplification of energy transfer can be extended over three vortices for a particular case of (p_1, p_2, p_3)=(1, −1, −1). We interpreted these remarkable observations using the temporal evolution of stray magnetic field and observed that antivortex packets moving through the stray field were accountable for the observed amplifications. The rules, which we postulated based upon the motion of the antivortex packets (or 'solitons') can also successfully explain the previous experimental observations in greater detail. We hope that further study of these solitons will aid the research community in creating a better analytical model which can predict such useful results as signal amplification without the need to do complete simulations.

Similar amplification may be observed in coupled mechanical oscillators. However, here the observed amplification in the energy transfer from left (input) to right (output) vortex for $(p_1, p_2, p_3) = (1, -1, -1)$ can be controlled by switching the polarity p_2 from 1 to -1, much like changing the states of a BJT between active and cut–off. This can be achieved by using a local magnetic field or a spin–polarized current; thus, making it a more suitable candidate for integration with current electronic technological ecosystem. Moreover the observed gain, while remaining constant at B_{active} for low signal strength h_0, drops dramatically for $h_0 > 0.25$ mT. Thus the output will not increase over a certain upper limit (76.61 dB for the MVT described here). This is similar to the saturation state of an electronic transistor. Direct parallels to all three operational states of a BJT, namely active, cut–off and saturation have thus been demonstrated for the discussed MVT. Also, both classic transistor operations of signal switching and amplification have been described. The dependence of gain characteristic, in particular B_{active} and B_{max} should be further explored with different material and geometrical parameters of the MVT and the driving signal frequency (dynamic response).

Our attempt to demonstrate a fan–out operation uncovered that the solitons involved in the dynamics do not split easily. This resulted in a higher level of asymmetry between different branches of a symmetrical network. This asymmetry was unlikely if the dynamic stray field lacked any of the topologically stable antivortices and treated both the branches evenly. This helped us to further validate the importance of antivortex solitons in the energy transfer mechanism. More work will be needed to demonstrate a successful fan–out operation by considering the cascade of antivortices for different network parameters.

Pinning, which can occur due to fabrication related issues, is known to affect the natural frequency of an isolated vortex.[344] However, as the dynamics studied here was forced, the observed results are expected to remain unaffected unless the pinning potential is high enough to change the trajectory of the vortex core or the cascade of solitons. A stronger pinning may sometimes occur at the Py–air boundary.[213] We have not considered this type of pinning here as it can affect the generation and dynamics of the stray field which is responsible for some of the reported observations. Thus, a different soft–ferromagnet may have to be used if pinning becomes an issue.

While advancing the cause of nano–electronic devices,[4] we also hope that these findings will promote the continued search of new and improved transistors.[345] For the type of transistor proposed here to become technologically viable and competitive, further research towards miniaturization and reduction of energy consumption and response delay are highly desirable.

13. Conclusions

In this thesis, we studied magnetization dynamics in nanoscale magnetic systems. Two types of closely related phenomena of spin–wave (SW) propagation and magnetic vortex gyration were studied as they fall in the microwave frequency band. The propagation of SW propagation was studied in thin–films, waveguides, one–dimensional (1D) and two–dimensional (2D) magnonic crystals (MCs). Time–resolved magneto–optic Kerr effect (TR–MOKE) based microscopy was used to experimentally study SWs in nanoscale magnonic waveguides. The magnetic vortex core can be made to gyrate in a closed cyclic loop by using an in–plane rotating excitation field. The dependence of the steady state of this gyrotropic motion on relative core polarities of magnetostatically coupled magnetic vortex network was also studied.

13.1. Summary

We start with developing a numerical framework to visualize and analyse the SW dynamics in different types nanoscale magnetic systems. In order to represent the magnetization data in frequency or wavevector domains, we used multi–domain Fourier transforms. We enhance our numerical techniques to overcome some of the artefacts that are conventionally associated with the Fourier transforms. As a result, we begin to obtain high quality analysis data output which helped us uncover some new phenomena. In Chap. 4, we highlight the use of DFT windows and sinc functions to control the spectral leakage and aliasing, respectively. The efficacies of the numerical methods were established by comparing the results they produced with those obtained by using other techniques.[79,213,315] In Chap. 7, we improve the technique to compute SW power and phase profile to account for a specific wavevector while ignoring the remainder of the wavevector domain. In Chap. 9, we ensure the framework is now able to compute SW dispersion relation for 2D MCs. This was done largely by designing a new excitation signal which was capable to exciting the entire SW spectrum without producing any spurious modes. Here, we also discussed how to numerically obtain the iso–frequency lines for a MC. In Chap. 10, we improve the framework further by mapping the magnetization data into the complex plane. This helped us uncover the existence of a magnonic bandgap in submillimetre wave band. While continuing to improve the framework on the one hand, we have also reported some remarkable observations on the other.

In Chap. 5, we compare the effects of pinned and free boundary conditions on the SW dispersion relations of a nanoscale magnonic antidot waveguide (MAW). Here we arrived at the conclusion that bandgaps can be opened more easily if magnetization dynamics at ferromagnet–air boundary is pinned. Pinning also shifted the SW band structure positively in the frequency domain. Thus, we learned that higher frequencies observed during experimental measurements may sometimes be related to this type of pinning.

In Chap. 6, we highlight the importance of the mirror symmetry of a magnonic antidot waveguide. First, we show that a small shift in the symmetrically placed row of antidots can cause the collapse of pre-existing magnonic bandgaps. Next, we demonstrate how similar collapse (of the magnonic bandgaps) can be engineered by employing an asymmetric bias magnetic field. Here, we observe that although, different bandgaps may have plural origins, their collapse can occur mainly due to a loss of degeneracy which was originally predicated upon the existence of mirror symmetry. We also show that intrinsic and extrinsic sources of asymmetry can be made to work against each other in order to selectively recover the pre-existing bandgaps. An analytical model to facilitate this procedure has also been developed. Thus, it can either be done consciously to alter the magnonic band structure of a MAW; or it can be used to rectify a systematic fabrication defect by calibrating the bias magnetic field of varying spatial profiles. The analytical model developed here was based on the discrete translational and the mirror symmetries of a crystal. Thus, the fundamentals behind the observations drawn here may be extended to other types of waves. The compensation effects should also be observable and usable in other systems outside the field of magnonics.[287–289]

It was known that the spectrum of dipole dominated SWs can be controlled by changing the shape of the scattering centres on larger length scales.[63] In Chap. 7, we observe how the antidot's geometry can influence the SW dispersion in a MAW. Antidots in the shape of regular polygons are used for this analysis. We demonstrate that the band structure of exchange dominated SWs can be altered by changing the antidot shape. This change is seen to be effective only when the shape of the antidot actually changes the profile of the neighbouring exchange field. Power and phase distribution profiles were used to understand the origin of SW bands and bandgaps in different cases. As direct bandgaps are more desirable, this understanding can be used to improve the design of MAWs. Especially, since the direct bandgaps seen here can be opened at the same antidot filling fraction by simply changing the orientation of the holes.

After considering the effects of boundary conditions, mirror symmetry and antidot shape, in Chap. 8, we consider the effects of other geometrical parameters on SW dispersion in a MAW. The parameters considered here are antidot's size and MAW's lattice constant and scale. We also revisited the effect of antidot shape while considering MAWs on a different scale. The results obtained here can allow us to further characterize and control the magnonic band structure in a MAW. While examining the effect of MAW's scale we gained additional insight into the influence that exchange and dipolar interactions wield in the formation of the magnonic band structure. Using the PWM, it was found that an increase in the scale of the MAW can reveal backward volume magnetostatic bands in the spectrum. These bands are characterized by anti–parallel phase and group velocities close to the BZ centre. Although, a stronger splitting of degenerate modes was observed here the formation of SW band structure occurred in a manner which was qualitatively comparable to the case of exchange dominated SWs.

This study was conducted under the pinned boundary conditions. It was noticed that the effect of pinning becomes more pronounced with increase in the size of the antidots. This can allow one to control the crosstalk between the two halves of the waveguide (sub–waveguides) to increase or reduce the splitting of the degenerate modes. When the antidots' size is small in comparison the lattice constant of the waveguide, lower SW modes were localized amidst the row of the antidots. We also noticed that as a MAW's lattice constant was increased it started to resemble a uniform waveguide. However, unlike in the case of a uniform waveguide, where the SW dispersion modes are parabolic, here they became flatter. This was due to the fact that an increase in the lattice constant caused the BZ boundaries to come closer. Thus, the anticrossing of modes at the BZ boundaries starts to occur more frequently resulting in a flattening of the SW dispersion modes.

As magnonic analogues of the electronic Fermi surfaces, iso–frequency lines can help us explore the SW dynamics in the wavevector space. In Chap. 9, the use of iso–frequency lines helped us underscore the anisotropy that existed between two mutually orthogonal SW propagation directions. We also explored the band structure of 2D MCs in more detail by analysing the mode profile of SWs using the power and phase analysis of the SW. In this chapter, we also noticed that SW dispersion in a square dot array was largely mediated by the dipole field even though the edge of the square dots and the lattice constant were only 6 nm and 9 nm, respectively. A negative group velocity associated with the first mode in the case of a backward volume magnetostatic configuration was observed here, and unlike the case described in Fig. 8.5, the upward curve associated with exchange dominated SWs was never registered.

In Chap. 11, we experimentally explore the tunability of SW band structure of MAWs based on their geometry and the bias magnetic field. As pump–probe based time–resolved Kerr effect (TR–MOKE) microscopy was used to observe the dynamics, the discussion here is limited to a very low wavevector regime. Thus, instead of obtaining an entire band structure, we get a few peaks associated with $k \to 0$. Based on the agreements (or the lack thereof) while comparing experimental and simulated results, we showed that SW modes, particularly the quantized modes, localized amidst the antidot array were more sensitive to any variance in the fabrication parameters. In contrast, the SW modes in the sub–waveguides were very stable and only manipulable by magnetic bias field's strength or direction. Edge mode of the waveguide was observed only in the Damon–Eshbach configuration and not in the backward volume configuration as the lateral edges were much farther away.

We also investigated magnetic vortex core gyration. It has a characteristic frequency in the low gigahertz and sub–gigahertz frequency bands. We first demonstrated that isolated magnetic vortices can transduce energy from rotating magnetic field to vortex core gyration. We also noted that core–switching here can be avoided if off–resonance signals of lower amplitudes are used. Although, one also needs to consider a trade–off between the time taken to achieve the steady state and an anharmonic beating that is observed here. Next, we uncovered gyration mode amplification in magnetostatically coupled magnetic vortices. As inertia in the case of magnetic vortex cores is a vector (gyrovector) – as opposed to a scalar in the case of a conventional coupled oscillator, we demonstrated that this amplification can be switched on or off (by switching vortex core polarities). Based on this finding we also demonstrate transistor like operational states using a three vortex sequence.

Since these observations could not be explained by the current analytical model, we started to examine the temporal evolution of the stray field. We then discovered that antivortex packets moving through the stray field could account for these observations. Consequently our attempt to demonstrate a conventional fan–out operation was unsuccessful as the involved antivortices were topologically stable and would not split to divide the power equally in the daughter branches. We note this higher level of asymmetry was unlikely if the dynamic stray field did not posses these antivortices. This successfully validated the importance of antivortex solitons in the energy transfer mechanism.

13.2. Future Scope

If some of the techniques described here are to indeed become useful in creating new technology, the first thing that needs to be addressed is the resolution of the fabrication processes. There is a clear and wide divide between the length–scales of magnetic systems which are fabricable and those that can be handled using finite element or finite difference based numerical methods that exist today. Even with the recent advances in fabrication techniques which can allow one to pattern with resolutions below 10 nm,[50,98–100,346] it is still not possible to fabricate very accurately. For example, as seen in Chap. 11 the patterned dimensions may vary by $\pm 10\%$. This was clearly seen to alter the spectrum of SW modes localized amidst the antidot array.

In Chap. 5, we pointed out that pinning (at the edges of a geometry) can cause bandgaps to appear even if the filling fraction of antidots is as low as 5%. However, pinning cannot be achieved reliably. The results presented in Chap. 11 appear to agree with results simulated without the pinned boundary condition. Pinning largely depends upon the surface magnetic anisotropy which can get accidentally altered[282] during the fabrication processes. Thus, further study is required with the aim to control the surface anisotropy during the fabrication techniques that are involved here.

In Chap. 6, we noticed how important the mirror symmetry of a waveguide is, as far as the band structure of exchange–dominated SWs are concerned. Similar investigation can be done for dipole–dominated SWs, after taking the inhomogeneity and anisotropy of the demagnetizing field[286] and the multi–mode character of waveguides[201] into account. This necessitates further research on this subject. Also, since the process of development of the analytical model presented here was dependent solely on the mirror and discrete translational symmetries of the MAW — a 1D MC, future research may be undertaken to develop similar models for photonic or phononic analogues.

MCs were studied in some detail in this work. Useful devices, such as an add–drop filter can be envisioned by using magnonic quasicrystals. Thus more work needs to conducted with crystals which do not feature perfect discrete translational symmetry.

While discussing the observed amplifications of the gyrotropic modes in Chap. 12, we mention (see Sec. A.1) that the present analytical model does not predict these results. We think that further study, guided by the analysis of the dynamic stray field, can help with the development of an analytical model capable of predicting these useful results. We also need to optimize the gain B, as defined in Eq. (12.1), by examining its dependence on various geometrical and material parameters and the nature of excitation frequency. In the absence of a more complete analytical model, one will presently need to rely on extensive simulations to accomplish this task.

More work will also be required in the future in order to miniaturize the single transistor. The 'magnetic vortex transistor' (MVT) described in Chap. 12, spans an area of about 750 nm $\times$ 250 nm with a thickness of 40 nm. These dimensions will have to be reduced by an order of magnitude in order to make the MVT as a more attractive substitute to the kinds of transistors used today. As the diameter of an isolated nanodisk, which can support a magnetic vortex cannot be reduced indefinitely, more fundamental research is required here. We also need to study the power consumption and efficiency of a MVT to minimize the losses during transistor operations.

Fan–out is required to facilitate the design of more complex circuits. Since the topologically stable antivortices, which appear to be responsible for the observed amplification, do not treat different branches of the circuit symmetrically, more work is required here. Perhaps a successful fan–out can be obtained by observing the cascade of the involved antivortices and rearranging the branches of the circuit accordingly.

A. Appendix

A.1. Supplementary Note for Chap. 12

For a pair of coupled harmonic oscillators featuring the same inertia, stiffness and damping, it is not possible to get an increased oscillation in one of the oscillators while the other one is being driven with a frequency close to the eigenfrequency of individual oscillators. Some close parallels can be drawn between such mechanical coupled oscillators and a pair of magnetostatically coupled vortices as shown in Fig. 12.1 (b). We write the following Thiele's equation for both the vortices identifying them with subscripts $i = 1$ (left vortex) or $i = 2$ (right vortex):

$$-\kappa \mathbf{r}_i + \mathbf{G}_i \times \mathbf{v}_i + \overleftrightarrow{\mathbf{D}} \cdot \mathbf{v}_i - \frac{\partial W_{\mathrm{int}}\left(\mathbf{r}_1, \mathbf{r}_2\right)}{\partial \mathbf{r}_i} + \mathbf{T}_{\mathrm{sig},i} = 0.$$

Here, κ is a stiffness factor which seeks to restore the displaced vortex core functioning much like the stiffness of a spring.[163] $\mathbf{G}_i = -Gp_i\hat{\mathbf{z}}$ $(G > 0)$,[163] is the inertia associated with i^{th} vortex core. Polarity $p_1 = 1$ and $p_2 = \pm 1$ depending upon the case under consideration. Although, $\mathbf{G}_i$ depends upon polarity, the term $\mathbf{G}_i \times \mathbf{v}_i$ does not. This is because, if the polarity p_i is switched, both $\mathbf{G}_i$ and $\mathbf{v}_i$ change to $-\mathbf{G}_i$ and $-\mathbf{v}_i$, respectively; thus, preserving the original cross product. In the case of isotropic damping, the term $\overleftrightarrow{\mathbf{D}} \cdot \mathbf{v}_i$ can be replaced with $D\mathbf{v}_i$, where D is a scalar independent of polarity.[163] Also,[151]

$$\mathbf{T}_{\mathrm{sig},i} = \begin{cases} \mu\left(\hat{\mathbf{z}} \times \mathbf{H}_{\mathrm{sig}}\right) & i = 1 \\ 0 & i = 2 \end{cases},$$

where, μ is a chirality dependent coupling constant and $\mathbf{H}_{\text{sig}}$ is an in plane excitation field rotating at frequency κ/G. It is important to consider this eigenfrequency because a transducer which is converting a magnetic field signal to vortex core gyration signal is likely to show significant peaks around it (see Fig. A.1 (e)). W_{int} is the interaction energy between the two vortices, which according to Ref. 149 is given as

$$W_{\text{int}} = c_1 c_2 \left(\eta_x x_1 x_2 - \eta_y y_1 y_2\right),$$

where, $c_1 = c_2 = 1$ for the CCW chiralities considered here and $\eta_{x,y}$ is the interaction coefficients depending upon certain geometrical and material parameters, but independent of relative polarity.

It has now been established that all the terms in the Thiele's equation, with the exception of the dissipation term, are independent of relative polarity p_2 of the vortices. The dependence of the dissipation term upon the direction of velocity does not affect the absolute value of gain r_2/r_1. Thus, according to this model, the gain r_2/r_1 should not depend upon polarity p_2. This deviates from the polarity dependent amplification presented here. In the case of analogous mechanical coupled oscillators, it would be possible to show such gain while driving at a frequency f ($\leq f_0$), if the inertia of the oscillator (which is not being driven directly) was changed from I to $-I$. However, that is a purely hypothetical consideration.

A.2. Supplementary Figures for Chap. 12

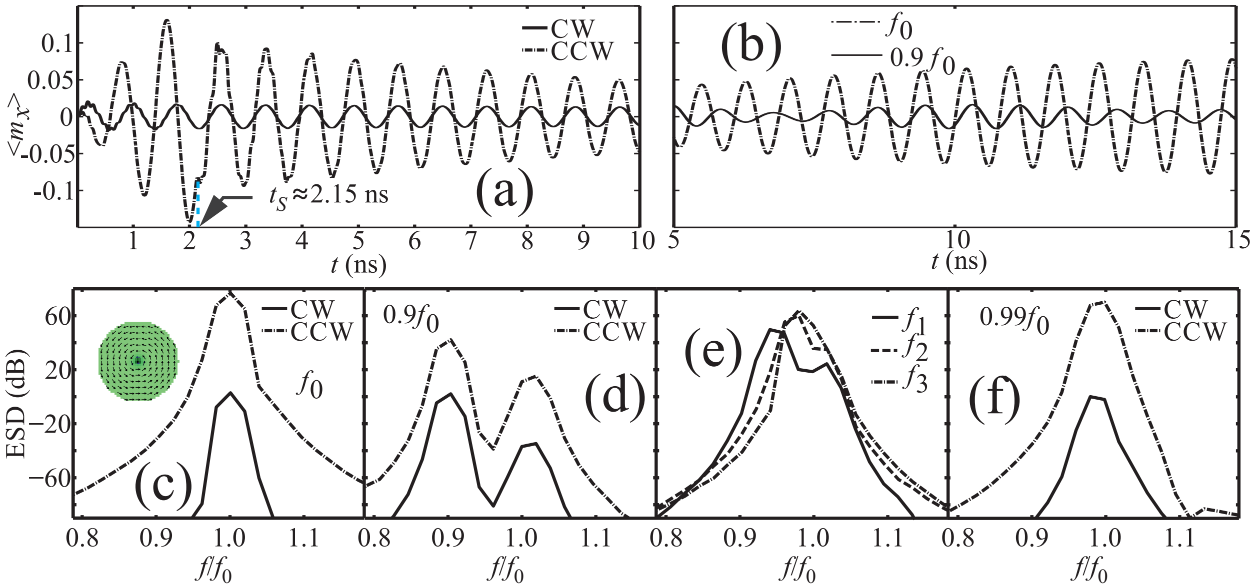

Figure A.1.: (a) Plots of $\langle m_x \rangle$ vs. time for signals rotating CW and CCW with a frequency f_0 and amplitude 1.5 mT. Polarity switching is seen with CCW signal at $t_s \approx 2.15$ ns. (b) Plots of $\langle m_x \rangle$ vs. time for signals rotating CCW with frequencies f_0 and $0.9f_0$ and amplitude 0.5 mT. No polarity switching is observed. Convergence for f_0 is taking more time. ESDs of vortex dynamics with excitation signal rotating CW and CCW with amplitude 0.5 mT and frequencies (c) f_0, (d) $0.9f_0$ and (f) $0.99f_0$. Beating is observed. Beating frequency decreases systematically with increasing signal frequency. (e) ESDs of vortex dynamics with excitation signal rotating CCW with amplitude 0.5 mT and frequencies $f_1 = 0.95f_0$, $f_1 = 0.975f_0$ and $f_1 = 0.98f_0$. As seen in the inset of (c), the core polarity is up and chirality is CCW.

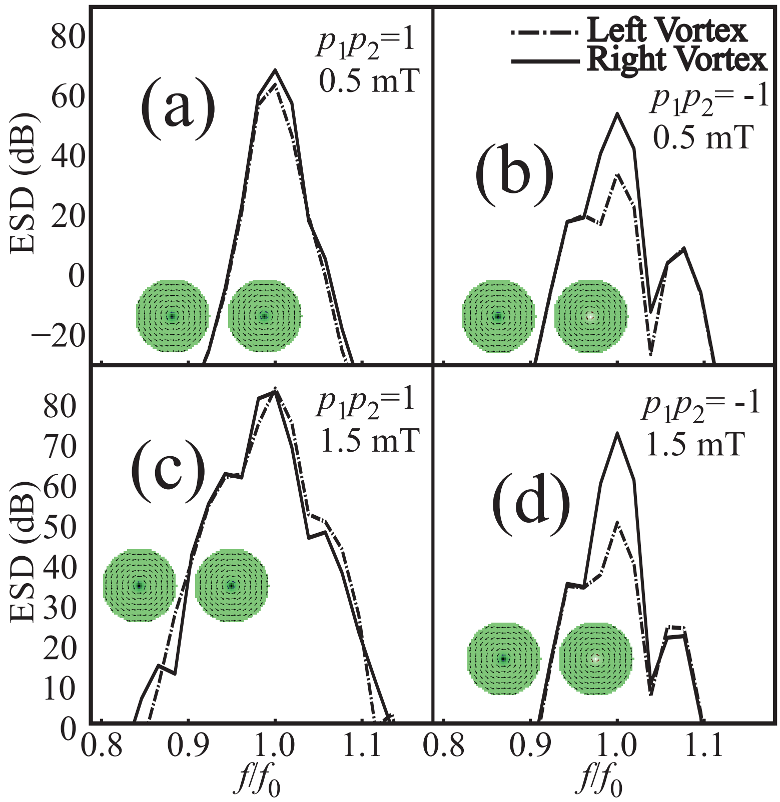

Figure A.2.: ESDs of left and right magnetic vortices shown in the insets with ((a) and (c)) similar and ((b) and (d)) opposite polarities while using a cell size of 2.5 nm × 2.5 nm × 40 nm. (a) and (b) show the results for a signal amplitude of 0.5 mT while (c) and (d) show those for an amplitude of 1.5 mT, both rotating CCW at $f = f_0$.

Bibliography

[1] F. Bloch, Z. Physik **61**, 206 (1930).

[2] F. J. Dyson, Phys. Rev. **102**, 1217 (1956).

[3] A. V. Chumak, V. S. Tiberkevich, A. D. Karenowska, A. A. Serga, J. F. Gregg, A. N. Slavin, and B. Hillebrands, Nat. Commun. **1**, 141 (2010).

[4] J. W. Kłos, D. Kumar, M. Krawczyk, and A. Barman, Sci. Rep. **3**, 2444 (2013).

[5] S.-K. Kim, J. Phys. D: Appl. Phys. **43**, 264004 (2010).

[6] B. Rana, *Quasistatic and Ultrafast Magnetization Dynamics in Magnetic Nanostructures*, Ph.D. thesis, University of Calcutta (2013).

[7] L. D. Landau and E. M. Lifshitz, Phys. Zeitsch. der Sow. **8**, 153 (1935).

[8] T. Gilbert, IEEE Trans. Mag. **40**, 3443 (2004).

[9] A. Barman, S. Barman, T. Kimura, Y. Fukuma, and Y. Otani, J. Phys. D: Appl. Phys. **43**, 422001 (2010).

[10] M. N. Baibich, J. M. Broto, A. Fert, F. N. Van Dau, F. Petroff, P. Etienne, G. Creuzet, A. Friederich, and J. Chazelas, Phys. Rev. Lett. **61**, 2472 (1988).

[11] G. Binasch, P. Grünberg, F. Saurenbach, and W. Zinn, Phys. Rev. B **39**, 4828 (1989).

[12] M. Inoue, K. Arai, T. Fujii, and M. Abe, J. Appl. Phys. **85**, 5768 (1999).

[13] P. F. Carcia, A. D. Meinhaldt, and A. Suna, Appl. Phys. Lett. **47**, 178 (1985).

[14] P. F. Carcia, J. Appl. Phys. **63**, 5066 (1988).

[15] S. Choi, K.-S. Lee, K. Y. Guslienko, and S.-K. Kim, Phys. Rev. Lett. **98**, 087205 (2007).

[16] S. Gliga, *Ultrafast Vortex Core Dynamics Investigated by Finite-element Micromagnetic Simulations*, Schriften des Forschungszentrums Jülich / Reihe Energie & Umwelt: Reihe Energie & Umwelt (Forschungszentrum Jülich, Zentralbibliothek, 2010).

[17] J. Bland and B. Heinrich, eds., *Ultrathin Magnetic Structures II*, Ultrathin Magnetic Structures (Springer, 2005).

[18] S. Iida, J. Phys. Chem. Solids **24**, 625 (1963).

[19] R. Arias and D. L. Mills, Phys. Rev. B **60**, 7395 (1999).

[20] J. Lindner, K. Lenz, E. Kosubek, K. Baberschke, D. Spoddig, R. Meckenstock, J. Pelzl, Z. Frait, and D. L. Mills, Phys. Rev. B **68**, 060102 (2003).

[21] J. Xiao, A. Zangwill, and M. D. Stiles, Phys. Rev. B **70**, 172405 (2004).

[22] T. Sebastian, Y. Ohdaira, T. Kubota, P. Pirro, T. Brächer, K. Vogt, A. A. Serga, H. Naganuma, M. Oogane, Y. Ando, and B. Hillebrands, Appl. Phys. Lett. **100**, 112402 (2012).

[23] A. Conca, J. Greser, T. Sebastian, S. Klingler, B. Obry, B. Leven, and B. Hillebrands, J. Appl. Phys. **113**, 213909 (2013).

[24] L. Zhang, J. Ren, J.-S. Wang, and B. Li, Phys. Rev. B **87**, 144101 (2013).

[25] R. Shindou, R. Matsumoto, S. Murakami, and J.-i. Ohe, Phys. Rev. B **87**, 174427 (2013).

[26] A. I. Akhierzer, V. G. Bar'yakhtar, and S. V. Peletminskii, *Spin Waves* (North–Holland, 1968).

[27] A. Gurevich and G. Melkov, *Magnetization Oscillations and Waves* (Taylor & Francis, 1996).

[28] D. Stancil and A. Prabhakar, *Spin Waves: Theory and Applications* (Springer, 2009).

[29] K.-J. Lee, A. Deac, O. Redon, J.-P. Nozieres, and B. Dieny, Nat. Mater. **3**, 877 (2004).

[30] T. Holstein and H. Primakoff, Phys. Rev. **58**, 1098 (1940).

[31] C. Rüegg, A. Furrer, D. Sheptyakov, T. Strässle, K. W. Krämer, H.-U. Güdel, and L. Mélési, Phys. Rev. Lett. **93**, 257201 (2004).

[32] S. O. Demokritov, V. E. Demidov, O. Dzyapko, G. A. Melkov, A. A. Serga, B. Hillebrands, and A. N. Slavin, Nature **443**, 430 (2006).

[33] P. Nowik-Boltyk, O. Dzyapko, V. E. Demidov, N. G. Berloff, and S. O. Demokritov, Sci. Rep. **2**, 482 (2012).

[34] G. Srivastava, *The Physics of Phonons* (Taylor & Francis, 1990).

[35] S. Nikitov, P. Tailhades, and C. Tsai, J. Magn. Magn. Mater. **236**, 320 (2001).

[36] H. Puszkarski and M. Krawczyk, Solid State Phenom. **94**, 125 (2003).

[37] S. Neusser and D. Grundler, Adv. Mater. **21**, 2927 (2009).

[38] B. Lenk, H. Ulrichs, F. Garbs, and M. Munzenberg, Physics Reports **507**, 107 (2011).

[39] L. J. Heyderman and R. L. Stamps, J. Phys.: Condens. Matter **25**, 363201 (2013).

[40] C. G. Sykes, J. D. Adam, and J. H. Collins, Appl. Phys. Lett. **29**, 388 (1976).

[41] C. Bayer, M. P. Kostylev, and B. Hillebrands, Appl. Phys. Lett. **88**, 112504 (2006).

[42] V. V. Kruglyak, R. J. Hicken, A. N. Kuchko, and V. Y. Gorobets, J. Appl. Phys. **98**, 014304 (2005).

[43] A. V. Chumak, A. A. Serga, B. Hillebrands, and M. P. Kostylev, Appl. Phys. Lett. **93**, 022508 (2008).

[44] Z. K. Wang, V. L. Zhang, H. S. Lim, S. C. Ng, M. H. Kuok, S. Jain, and A. O. Adeyeye, Appl. Phys. Lett. **94**, 083112 (2009).

[45] S. Mamica, M. Krawczyk, and J. W. Kłos, Adv. Cond. Matt. Phys. **2012**, 161387 (2012).

[46] S. Vysotskii, S. Nikitov, E. Pavlov, and Y. Filimonov, J. Commun. Technol. Electron. **55**, 800 (2010).

[47] S. Tacchi, M. Madami, G. Gubbiotti, G. Carlotti, H. Tanigawa, T. Ono, and M. P. Kostylev, Phys. Rev. B **82**, 024401 (2010).

[48] S. Tacchi, F. Montoncello, M. Madami, G. Gubbiotti, G. Carlotti, L. Giovannini, R. Zivieri, F. Nizzoli, S. Jain, A. O. Adeyeye, and N. Singh, Phys. Rev. Lett. **107**, 127204 (2011).

[49] S. Saha, S. Barman, J. Ding, A. O. Adeyeye, and A. Barman, Appl. Phys. Lett. **102**, 242409 (2013).

[50] R. Mandal, S. Saha, D. Kumar, S. Barman, S. Pal, K. Das, A. K. Raychaudhuri, Y. Fukuma, Y. Otani, and A. Barman, ACS Nano **6**, 3397 (2012).

[51] M. Krawczyk and H. Puszkarski, Phys. Rev. B **77**, 054437 (2008).

[52] S. Mamica, M. Krawczyk, M. L. Sokolovskyy, and J. Romero-Vivas, Phys. Rev. B **86**, 144402 (2012).

[53] M. J. Pechan, C. Yu, R. L. Compton, J. P. Park, and P. A. Crowell, J. Appl. Phys. **97**, 10J903 (2005).

[54] S. Neusser, B. Botters, and D. Grundler, Phys. Rev. B **78**, 054406 (2008).

[55] S. Neusser, G. Duerr, H. G. Bauer, S. Tacchi, M. Madami, G. Woltersdorf, G. Gubbiotti, C. H. Back, and D. Grundler, Phys. Rev. Lett. **105**, 067208 (2010).

[56] S. Tacchi, M. Madami, G. Gubbiotti, G. Carlotti, A. Adeyeye, S. Neusser, B. Botters, and D. Grundler, IEEE Trans. Magn. **46**, 1440 (2010).

[57] S. Neusser, H. G. Bauer, G. Duerr, R. Huber, S. Mamica, G. Woltersdorf, M. Krawczyk, C. H. Back, and D. Grundler, Phys. Rev. B **84**, 184411 (2011).

[58] S. Tacchi, B. Botters, M. Madami, J. W. Kłos, M. L. Sokolovskyy, M. Krawczyk, G. Gubbiotti, G. Carlotti, A. O. Adeyeye, S. Neusser, and D. Grundler, Phys. Rev. B **86**, 014417 (2012).

[59] C.-L. Hu, R. Magaraggia, H.-Y. Yuan, C. S. Chang, M. Kostylev, D. Tripathy, A. O. Adeyeye, and R. L. Stamps, Appl. Phys. Lett. **98**, 262508 (2011).

[60] Z. K. Wang, V. L. Zhang, H. S. Lim, S. C. Ng, M. H. Kuok, S. Jain, and A. O. Adeyeye, ACS Nano **4**, 643 (2010).

[61] G. Duerr, M. Madami, S. Neusser, S. Tacchi, G. Gubbiotti, G. Carlotti, and D. Grundler, Appl. Phys. Lett. **99**, 202502 (2011).

[62] S. Tacchi, G. Duerr, J. W. Klos, M. Madami, S. Neusser, G. Gubbiotti, G. Carlotti, M. Krawczyk, and D. Grundler, Phys. Rev. Lett. **109**, 137202 (2012).

[63] J. W. Kłos, M. L. Sokolovskyy, S. Mamica, and M. Krawczyk, J. Appl. Phys. **111**, 123910 (2012).

[64] S. Saha, R. Mandal, S. Barman, D. Kumar, B. Rana, Y. Fukuma, S. Sugimoto, Y. Otani, and A. Barman, Adv. Funct. Mater. **23**, 2378 (2013).

[65] R. Mandal, P. Laha, K. Das, S. Saha, S. Barman, A. K. Raychaudhuri, and A. Barman, Appl. Phys. Lett. **103**, 262410 (2013).

[66] J. W. Kłos, D. Kumar, M. Krawczyk, and A. Barman, Phys. Rev. B **89**, 014406 (2014).

[67] R. Zivieri, S. Tacchi, F. Montoncello, L. Giovannini, F. Nizzoli, M. Madami, G. Gubbiotti, G. Carlotti, S. Neusser, G. Duerr, and D. Grundler, Phys. Rev. B **85**, 012403 (2012).

[68] D. Kumar, P. Sabareesan, W. Wang, H. Fangohr, and A. Barman, J. Appl. Phys. **114**, 023910 (2013).

[69] V. V. Kruglyak, S. O. Demokritov, and D. Grundler, J. Phys. D: Appl. Phys. **43**, 264001 (2010).

[70] A. A. Serga, A. V. Chumak, and B. Hillebrands, J. Phys. D: Appl. Phys. **43**, 264002 (2010).

[71] S. O. Demokritov and A. N. Slavin, *Magnonics: From Fundamentals to Applications* (Springer, 2013).

[72] T. Schneider, A. Serga, B. Hillebrands, and M. Kostylev, J. Nanoelectr. Optoelectr. **3**, 69 (2008).

[73] F. Macià, A. D. Kent, and F. C. Hoppensteadt, Nanotechnology **22**, 095301 (2011).

[74] A. Khitun, M. Bao, and K. L. Wang, J. Phys. D: Appl. Phys. **43**, 264005 (2010).

[75] R. V. Mikhaylovskiy, E. Hendry, and V. V. Kruglyak, Phys. Rev. B **82**, 195446 (2010).

[76] H. Rong, S. Xu, O. Cohen, O. Raday, M. Lee, V. Sih, and M. Paniccia, Nat. Photon. **2**, 170 (2008).

[77] A. Khitun, M. Bao, and K. Wang, IEEE Trans. Mag. **44**, 2141 (2008).

[78] H. Yu, G. Duerr, R. Huber, M. Bahr, T. Schwarze, F. Brandl, and D. Grundler, Nat. Commun. **4**, 2702 (2013).

[79] G. Venkat, D. Kumar, M. Franchin, O. Dmytriiev, M. Mruczkiewicz, H. Fangohr, A. Barman, M. Krawczyk, and A. Prabhakar, IEEE Trans. Mag. **49**, 524 (2013).

[80] S. Choi, K.-S. Lee, and S.-K. Kim, Appl. Phys. Lett. **89**, 062501 (2006).

[81] J. Podbielski, F. Giesen, and D. Grundler, Phys. Rev. Lett. **96**, 167207 (2006).

[82] T. Schneider, A. A. Serga, B. Leven, B. Hillebrands, R. L. Stamps, and M. P. Kostylev, Appl. Phys. Lett. **92**, 022505 (2008).

[83] Y. Au, M. Dvornik, O. Dmytriiev, and V. V. Kruglyak, Appl. Phys. Lett. **100**, 172408 (2012).

[84] K.-S. Lee, D.-S. Han, and S.-K. Kim, Phys. Rev. Lett. **102**, 127202 (2009).

[85] S.-K. Kim, K.-S. Lee, and D.-S. Han, Appl. Phys. Lett. **95**, 082507 (2009).

[86] F. Ciubotaru, A. V. Chumak, N. Y. Grigoryeva, A. A. Serga, and B. Hillebrands, J. Phys. D: Appl. Phys. **45**, 255002 (2012).

[87] A. Khitun, J. Appl. Phys. **111**, 054307 (2012).

[88] S. Bonetti, P. Muduli, F. Mancoff, and J. Åkerman, Appl. Phys. Lett. **94**, 102507 (2009).

[89] O. Prokopenko, E. Bankowski, T. Meitzler, V. Tiberkevich, and A. Slavin, IEEE Magn. Lett. **2**, 3000104 (2011).

[90] M. Madami, S. Bonetti, G. Consolo, S. Tacchi, G. Carlotti, G. Gubbiotti, F. B., Mancoff, M. A. Yar, and J. Åkerman, Nat. Nanotechnol. **6**, 635 (2011).

[91] T. Satoh, Y. Terui, R. Moriya, B. A. Ivanov, K. Ando, E. Saitoh, T. Shimura, and K. Kuroda, Nat. Photon. **6**, 662 (2012).

[92] A. Kozhanov, D. Ouellette, Z. Griffith, M. Rodwell, A. Jacob, D. Lee, S. Wang, and S. Allen, Appl. Phys. Lett. **94**, 012505 (2009).

[93] V. E. Demidov, M. P. Kostylev, K. Rott, J. Munchenberger, G. Reiss, and S. O. Demokritov, Appl. Phys. Lett. **99**, 082507 (2011).

[94] L. Bai, M. Kohda, and J. Nitta, Appl. Phys. Lett. **98**, 172508 (2011).

[95] P. Clausen, K. Vogt, H. Schultheiss, S. Schafer, B. Obry, G. Wolf, P. Pirro, B. Leven, and B. Hillebrands, Appl. Phys. Lett. **99**, 162505 (2011).

[96] G. Duerr, K. Thurner, J. Topp, R. Huber, and D. Grundler, Phys. Rev. Lett. **108**, 227202 (2012).

[97] T. Schwarze, R. Huber, G. Duerr, and D. Grundler, Phys. Rev. B **85**, 134448 (2012).

[98] F. H. M. Rahman, S. McVey, L. Farkas, J. A. Notte, S. Tan, and R. H. Livengood, Scanning **34**, 129 (2012).

[99] V. Sidorkin, E. van Veldhoven, E. van der Drift, P. Alkemade, H. Salemink, and D. Maas, J. Vac. Sci. Technol. B **27**, L18 (2009).

[100] T. G. Siegfried, Y. Ekinci, H. H. Solak, O. J. F. Martin, and H. Sigg, Appl. Phys. Lett. **99**, 263302 (2011).

[101] T. Silva and W. Rippard, J. Magn. Magn. Mater. **320**, 1260 (2008).

[102] R. E. Camley and R. L. Stamps, eds., *Chapter Four - Spin-Torque Oscillators*, Solid State Physics, Vol. 63 (Academic Press, 2012) pp. 217 – 294.

[103] S. I. Kiselev, J. C. Sankey, I. N. Krivorotov, N. C. Emley, R. J. Schoelkopf, R. A. Buhrman, and D. C. Ralph, Nature **425**, 380 (2003).

[104] J. E. Hirsch, Phys. Rev. Lett. **83**, 1834 (1999).

[105] K. Uchida, S. Takahashi, K. Harii, J. Ieda, W. Koshibae, K. Ando, S. Maekawa, and E. Saitoh, Nature **455**, 778 (2008).

[106] C. M. Jaworski, J. Yang, S. Mack, D. D. Awschalom, J. P. Heremans, and R. C. Myers, Nat. Mater. **9**, 898 (2010).

[107] H. Adachi, K. ichi Uchida, E. Saitoh, and S. Maekawa, Rep. on Prog. in Phys. **76**, 036501 (2013).

[108] M. Agrawal, V. I. Vasyuchka, A. A. Serga, A. D. Karenowska, G. A. Melkov, and B. Hillebrands, Phys. Rev. Lett. **111**, 107204 (2013).

[109] B. F. Miao, S. Y. Huang, D. Qu, and C. L. Chien, Phys. Rev. Lett. **111**, 066602 (2013).

[110] A. V. Kimel, A. Kirilyuk, A. Tsvetkov, R. V. Pisarev, and T. Rasing, Nature **429**, 850 (2004).

[111] K. Perzlmaier, M. Buess, C. H. Back, V. E. Demidov, B. Hillebrands, and S. O. Demokritov, Phys. Rev. Lett. **94**, 057202 (2005).

[112] A. V. Kimel, A. Kirilyuk, F. Hansteen, R. V. Pisarev, and T. Rasing, J. Phys.: Condens. Matter **19**, 043201 (2007).

[113] J.-Y. Bigot, M. Vomir, and E. Beaurepaire, Nat. Phys. **5**, 515 (2009).

[114] Y. Gong, A. R. Kutayiah, X. H. Zhang, J. H. Zhao, and Y. H. Ren, J. Appl. Phys. **111**, 07D505 (2012).

[115] W. K. Hiebert, A. Stankiewicz, and M. R. Freeman, Phys. Rev. Lett. **79**, 1134 (1997).

[116] A. Barman, V. V. Kruglyak, R. J. Hicken, A. Kundrotaite, and M. Rahman, Appl. Phys. Lett. **82**, 3065 (2003).

[117] B. Rana and A. Barman, SPIN **03**, 1330001 (2013).

[118] Y. Zhang, T.-H. Chuang, K. Zakeri, and J. Kirschner, Phys. Rev. Lett. **109**, 087203 (2012).

[119] D. Polley, A. Ganguly, A. Barman, and R. K. Mitra, Opt. Lett. **38**, 2754 (2013).

[120] T. Kampfrath, A. Sell, G. Klatt, A. Pashkin, S. Mahrlein, T. Dekorsy, M. Wolf, M. Fiebig, A. Leitenstorfer, and R. Huber, Nat. Photon. **5**, 31 (2011).

[121] J. Nishitani, T. Nagashima, and M. Hangyo, Phys. Rev. B **85**, 174439 (2012).

[122] T. J. Silva, C. S. Lee, T. M. Crawford, and C. T. Rogers, J. Appl. Phys. **85**, 7849 (1999).

[123] G. Counil, J.-V. Kim, T. Devolder, C. Chappert, K. Shigeto, and Y. Otani, J. Appl. Phys. **95**, 5646 (2004).

[124] S. Demokritov, B. Hillebrands, and A. Slavin, Phys. Rep. **348**, 441 (2001).

[125] C. L. Ordóñez Romero, M. A. Cherkasskii, N. Qureshi, B. A. Kalinikos, and C. E. Patton, Phys. Rev. B **87**, 174430 (2013).

[126] R. Antos, Y. Otani, and J. Shibata, J. Phys. Soc. Jpn. **77**, 031004 (2008).

[127] K. Y. Guslienko, K.-S. Lee, and S.-K. Kim, Phys. Rev. Lett. **100**, 027203 (2008).

[128] B. Van Waeyenberge, A. Puzic, H. Stoll, K. W. Chou, T. Tyliszczak, R. Hertel, M. Fahnle, H. Bruckl, K. Rott, G. Reiss, I. Neudecker, D. Weiss, C. H. Back, and G. Schutz, Nature **444**, 461 (2006).

[129] K. Yamada, S. Kasai, Y. Nakatani, K. Kobayashi, H. Kohno, A. Thiaville, and T. Ono, Nat. Mater. **6**, 270 (2007).

[130] R. P. Cowburn, Nat. Mater. **6**, 255 (2007).

[131] J. Thomas, Nat. Nanotechnol. **2**, 206 (2007).

[132] R. Cowburn, J. Magn. Magn. Mater. **242–245**, 505 (2002).

[133] J. A. J. Burgess, A. E. Fraser, F. F. Sani, D. Vick, B. D. Hauer, J. P. Davis, and M. R. Freeman, Science **339**, 1051 (2013).

[134] A. Wachowiak, J. Wiebe, M. Bode, O. Pietzsch, M. Morgenstern, and R. Wiesendanger, Science **298**, 577 (2002).

[135] T. Shinjo, T. Okuno, R. Hassdorf, . K. Shigeto, and T. Ono, Science **289**, 930 (2000).

[136] M. R. Pufall, W. H. Rippard, S. E. Russek, S. Kaka, and J. A. Katine, Phys. Rev. Lett. **97**, 087206 (2006).

[137] K. Y. Guslienko, B. A. Ivanov, V. Novosad, Y. Otani, H. Shima, and K. Fukamichi, J. Appl. Phys. **91**, 8037 (2002).

[138] S.-B. Choe, Y. Acremann, A. Scholl, A. Bauer, A. Doran, J. StÃűhr, and H. A. Padmore, Science **304**, 420 (2004).

[139] S. Sugimoto, Y. Fukuma, S. Kasai, T. Kimura, A. Barman, and Y. Otani, Phys. Rev. Lett. **106**, 197203 (2011).

[140] A. Vansteenkiste, K. W. Chou, M. Weigand, M. Curcic, V. Sackmann, H. Stoll, T. Tyliszczak, G. Woltersdorf, C. H. Back, G. Schutz, and B. Van Waeyenberge, Nat. Phys. **5**, 332 (2009).

[141] M. Curcic, B. Van Waeyenberge, A. Vansteenkiste, M. Weigand, V. Sackmann, H. Stoll, M. Fähnle, T. Tyliszczak, G. Woltersdorf, C. H. Back, and G. Schütz, Phys. Rev. Lett. **101**, 197204 (2008).

[142] M. Weigand, B. Van Waeyenberge, A. Vansteenkiste, M. Curcic, V. Sackmann, H. Stoll, T. Tyliszczak, K. Kaznatcheev, D. Bertwistle, G. Woltersdorf, C. H. Back, and G. Schütz, Phys. Rev. Lett. **102**, 077201 (2009).

[143] M. Bolte, G. Meier, B. Krüger, A. Drews, R. Eiselt, L. Bocklage, S. Bohlens, T. Tyliszczak, A. Vansteenkiste, B. Van Waeyenberge, K. W. Chou, A. Puzic, and H. Stoll, Phys. Rev. Lett. **100**, 176601 (2008).

[144] B. L. Mesler, K. S. Buchanan, M.-Y. Im, and P. Fischer, J. Appl. Phys. **111**, 07D311 (2012).

[145] K.-S. Lee and S.-K. Kim, Appl. Phys. Lett. **91**, 132511 (2007).

[146] A. A. Thiele, Phys. Rev. Lett. **30**, 230 (1973).

[147] V. Novosad, F. Y. Fradin, P. E. Roy, K. S. Buchanan, K. Y. Guslienko, and S. D. Bader, Phys. Rev. B **72**, 024455 (2005).

[148] Y. Liu, S. Gliga, R. Hertel, and C. M. Schneider, Appl. Phys. Lett. **91**, 112501 (2007).

[149] J. Shibata, K. Shigeto, and Y. Otani, Phys. Rev. B **67**, 224404 (2003).

[150] J. Shibata and Y. Otani, Phys. Rev. B **70**, 012404 (2004).

[151] K. Y. Guslienko, Appl. Phys. Lett. **89**, 022510 (2006).

[152] K.-S. Lee and S.-K. Kim, Phys. Rev. B **78**, 014405 (2008).

[153] K. L. Metlov and K. Y. Guslienko, J. Magn. Magn. Mater. **242–245**, 1015 (2002), proceedings of the Joint European Magnetic Symposia (JEMS'01).

[154] K.-S. Lee, H. Jung, D.-S. Han, and S.-K. Kim, J. Appl. Phys. **110**, 113903 (2011).

[155] H. Jung, K.-S. Lee, D.-E. Jeong, Y.-S. Choi, Y.-S. Yu, D.-S. Han, A. Vogel, L. Bocklage, G. Meier, M.-Y. Im, P. Fischer, and S.-K. Kim, Sci. Rep. **1**, (2011).

[156] A. Vogel, T. Kamionka, M. Martens, A. Drews, K. W. Chou, T. Tyliszczak, H. Stoll, B. Van Waeyenberge, and G. Meier, Phys. Rev. Lett. **106**, 137201 (2011).

[157] A. Vogel, A. Drews, M. Weigand, and G. Meier, AIP Advances **2**, 042180 (2012).

[158] L. Landau and E. Lifshits, Ukr. J. Phys. **53**, 14 (2008).

[159] B. Krüger, A. Drews, M. Bolte, U. Merkt, D. Pfannkuche, and G. Meier, Phys. Rev. B **76**, 224426 (2007).

[160] S. Barman, A. Barman, and Y. Otani, IEEE Trans. Magn. **46**, 1342 (2010).

[161] S. Barman, A. Barman, and Y. Otani, J. Phys. D: Appl. Phys. **43**, 335001 (2010).

[162] H. Jung, Y.-S. Choi, K.-S. Lee, D.-S. Han, Y.-S. Yu, M.-Y. Im, P. Fischer, and S.-K. Kim, ACS Nano **6**, 3712 (2012).

[163] J.-H. Kim, K.-S. Lee, H. Jung, D.-S. Han, and S.-K. Kim, Appl. Phys. Lett. **101**, 092403 (2012).

[164] A. Morrish, *The Physical Principles of Magnetism*, An IEEE Press classic reissue (Wiley, 2001).

[165] R. O'Handley, *Modern Magnetic Materials: Principles and Applications*, A Wiley-Interscience publication (Wiley, 1999).

[166] G. Bordignon, *Simulations of ferromagnetic nano–structures*, Ph.D. thesis, University of Southampton (2008).

[167] A. Aharoni, *Introduction to the Theory of Ferromagnetism*, International Series of Monographs on Physics (Clarendon Press, 2000).

[168] M. Oogane, T. Wakitani, S. Yakata, R. Yilgin, Y. Ando, A. Sakuma, and T. Miyazaki, Jpn. J. Appl. Phys. **45**, 3889 (2006).

[169] S. Trudel, O. Gaier, J. Hamrle, and B. Hillebrands, J. Phys. D: Appl. Phys. **43**, 193001 (2010).

[170] C. Scheck, L. Cheng, and W. E. Bailey, Appl. Phys. Lett. **88**, 252510 (2006).

[171] A. Knittel, *Micromagnetic simulations of three dimensional core-shell nanostructures*, Ph.D. thesis, University of Southampton (2011).

[172] J. H. E. Griffiths, Nature **158**, 670 (1946).

[173] C. Kittel, Phys. Rev. **73**, 155 (1948).

[174] A. Hubert and R. Schäfer, *Magnetic Domains: The Analysis of Magnetic Microstructures* (Springer, 1998).

[175] E. Beaurepaire, J.-C. Merle, A. Daunois, and J.-Y. Bigot, Phys. Rev. Lett. **76**, 4250 (1996).

[176] B. Koopmans, Nat. Mater. **6**, 715 (2007).

[177] E. Carpene, E. Mancini, C. Dallera, M. Brenna, E. Puppin, and S. De Silvestri, Phys. Rev. B **78**, 174422 (2008).

[178] J.-Y. Bigot, M. Vomir, L. Andrade, and E. Beaurepaire, Chemical Physics **318**, 137 (2005).

[179] L. Guidoni, E. Beaurepaire, and J.-Y. Bigot, Phys. Rev. Lett. **89**, 017401 (2002).

[180] P. M. Oppeneer and A. Liebsch, J. Phys. Condens. Matter **16**, 5519 (2004).

[181] G. P. Zhang and W. Hübner, Phys. Rev. Lett. **85**, 3025 (2000).

[182] E. Beaurepaire, G. M. Turner, S. M. Harrel, M. C. Beard, J.-Y. Bigot, and C. A. Schmuttenmaer, Appl. Phys. Lett. **84**, 3465 (2004).

[183] M. Battiato, K. Carva, and P. M. Oppeneer, Phys. Rev. Lett. **105**, 027203 (2010).

[184] A. Eschenlohr, M. Battiato, P. Maldonado, N. Pontius, T. Kachel, K. Holldack, R. Mitzner, A. Föhlisch, P. M. Oppeneer, and C. Stamm, Nat. Mater. **12**, 332 (2013).

[185] B. Koopmans, J. J. M. Ruigrok, F. D. Longa, and W. J. M. de Jonge, Phys. Rev. Lett. **95**, 267207 (2005).

[186] M. Krauß, T. Roth, S. Alebrand, D. Steil, M. Cinchetti, M. Aeschlimann, and H. C. Schneider, Phys. Rev. B **80**, 180407 (2009).

[187] G. P. Zhang, W. Hubner, G. Lefkidis, Y. Bai, and T. F. George, Nat. Phys. **5**, 499 (2009).

[188] B. Koopmans, G. Malinowski, F. Dalla Longa, D. Steiauf, M. Fahnle, T. Roth, M. Cinchetti, and M. Aeschlimann, Nat. Mater. **9**, 259 (2010).

[189] A. Laraoui, V. Halté, M. Vomir, J. Vénuat, M. Albrecht, E. Beaurepaire, and J.-Y. Bigot, The European Physical Journal D **43**, 251 (2007).

[190] A. Laraoui, J. Vénuat, V. Halté, M. Albrecht, E. Beaurepaire, and J.-Y. Bigot, Journal of Applied Physics **101**, 09C105 (2007).

[191] F. Goedsche, Phys. Status Solidi B **39**, K29 (1970).

[192] J. Gouzerh, A. A. Stashkevich, N. G. Kovshikov, V. V. Matyushev, and J. M. Desvignes, Journal of Magnetism and Magnetic Materials **101**, 189 (1991).

[193] Y. I. Gorobets and S. A. Reshetnyak, Tech. Phys. **43**, 188 (1998).

[194] A. V. Vashkovskii and E. H. Lokk, Phys.–Usp. **47**, 601 (2004).

[195] S.-K. Kim, S. Choi, K.-S. Lee, D.-S. Han, D.-E. Jung, and Y.-S. Choi, Appl. Phys. Lett. **92**, 212501 (2008).

[196] V. E. Demidov, S. O. Demokritov, D. Birt, B. O'Gorman, M. Tsoi, and X. Li, Phys. Rev. B **80**, 014429 (2009).

[197] P. A. Fleury, S. P. S. Porto, L. E. Cheesman, and H. J. Guggenheim, Phys. Rev. Lett. **17**, 84 (1966).

[198] V. K. Dugaev, P. Bruno, B. Canals, and C. Lacroix, Phys. Rev. B **72**, 024456 (2005).

[199] S. Yang, Z. Song, and C. P. Sun, Eur. Phys. J. B **52**, 377 (2006).

[200] K. Perzlmaier, G. Woltersdorf, and C. H. Back, Phys. Rev. B **77**, 054425 (2008).

[201] D. R. Birt, B. OGorman, M. Tsoi, X. Li, V. E. Demidov, and S. O. Demokritov, Appl. Phys. Lett. **95**, 122510 (2009).

[202] S. O. Demokritov, A. A. Serga, A. André, V. E. Demidov, M. P. Kostylev, B. Hillebrands, and A. N. Slavin, Phys. Rev. Lett. **93**, 047201 (2004).

[203] A. Kozhanov, D. Ouellette, M. Rodwell, S. J. Allen, A. P. Jacob, D. W. Lee, and S. X. Wang, J. Appl. Phys. **105**, 07D311 (2009).

[204] E. Vilkov, Phys. Solid State **48**, 1754 (2006).

[205] D. D. Stancil, B. E. Henty, A. G. Cepni, and J. P. Van't Hof, Phys. Rev. B **74**, 060404 (2006).

[206] V. Vlaminck and M. Bailleul, Science **322**, 410 (2008).

[207] A. M. Kosevich, B. A. Ivanov, and A. S. Kovalev, Phys. Rep. **194**, 117 (1990).

[208] Y. K. Fetisov, C. E. Patton, and V. T. Synogach, JETP Lett. **83**, 488 (2006).

[209] M. Wu, P. Krivosik, B. A. Kalinikos, and C. E. Patton, Phys. Rev. Lett. **96**, 227202 (2006).

[210] Y. M. Bunkov and G. E. Volovik, J. Low Temp. Phys. **150**, 135 (2008).

[211] C. Kittel, *Introduction to solid state physics* (Wiley, 1976).

[212] H. Kronmüller and S. Parkin, *Handbook of magnetism and advanced magnetic materials: Micromagnetism*, Handbook of Magnetism and Advanced Magnetic Materials (John Wiley & Sons, 2007).

[213] J. W. Kłos, D. Kumar, J. Romero-Vivas, H. Fangohr, M. Franchin, M. Krawczyk, and A. Barman, Phys. Rev. B **86**, 184433 (2012).

[214] B. A. Kalinikos and A. N. Slavin, J. Phys. C: Solid State Phys. **19**, 7013 (1986).

[215] K. Y. Guslienko, S. O. Demokritov, B. Hillebrands, and A. N. Slavin, Phys. Rev. B **66**, 132402 (2002).

[216] F. Morgenthaler, Proc. IEEE **76**, 138 (1988).

[217] J. O. Vasseur, L. Dobrzynski, B. Djafari-Rouhani, and H. Puszkarski, Phys. Rev. B **54**, 1043 (1996).

[218] E. Feldtkeller and H. Thomas, Phys. Kondens. Materie **4**, 8 (1965).

[219] N. Usov and S. Peschany, J. Magn. Magn. Mater. **118**, L290 (1993).

[220] J. Bland and B. Heinrich, *Ultrathin Magnetic Structures IV: Applications of Nanomagnetism*, Ultrathin Magnetic Structures (Springer, 2005).

[221] J. K. Ha, R. Hertel, and J. Kirschner, Phys. Rev. B **67**, 224432 (2003).

[222] S. Parkin, Appl. Phys. Lett. **61**, 1358 (1992).

[223] E. Shuryak, *The QCD Vacuum, Hadrons and Superdense Matter*, Lecture Notes in Physics Series (World Scientific, 2004).

[224] G.-W. Chern, H. Youk, and O. Tchernyshyov, J. Appl. Phys. **99**, 08Q505 (2006).

[225] A. A. Belavin and A. M. Polyakov, JETP Lett. **22**, 245 (1975).

[226] T. Senthil, A. Vishwanath, L. Balents, S. Sachdev, and M. P. A. Fisher, Science **303**, 1490 (2004).

[227] F. Bloch, Phys. Rev. **70**, 460 (1946).

[228] K.-S. Lee, S. Choi, and S.-K. Kim, Appl. Phys. Lett. **87**, 192502 (2005).

[229] R. Hertel, S. Gliga, M. Fähnle, and C. M. Schneider, Phys. Rev. Lett. **98**, 117201 (2007).

[230] N. Kikuchi, S. Okamoto, O. Kitakami, Y. Shimada, S. G. Kim, Y. Otani, and K. Fukamichi, J. Appl. Phys. **90**, 6548 (2001).

[231] A. Malozemoff and J. Slonczewski, *Magnetic domain walls in bubble materials*, Applied solid state science: Supplement (Academic Press, 1979).

[232] D. L. Huber, J. Appl. Phys. **53**, 1899 (1982).

[233] D. L. Huber, Phys. Rev. B **26**, 3758 (1982).

[234] K. Y. Guslienko, V. Novosad, Y. Otani, H. Shima, and K. Fukamichi, Appl. Phys. Lett. **78**, 3848 (2001).

[235] K. Y. Guslienko, X. F. Han, D. J. Keavney, R. Divan, and S. D. Bader, Phys. Rev. Lett. **96**, 067205 (2006).

[236] M. Kläui, C. A. F. Vaz, J. A. C. Bland, W. Wernsdorfer, G. Faini, E. Cambril, and L. J. Heyderman, Applied Physics Letters **83**, 105 (2003).

[237] J. Shibata, Y. Nakatani, G. Tatara, H. Kohno, and Y. Otani, Phys. Rev. B **73**, 020403 (2006).

[238] L. Berger, Phys. Rev. B **33**, 1572 (1986).

[239] J. Shibata, Y. Nakatani, G. Tatara, H. Kohno, and Y. Otani, J. Magn. Magn. Mater. **310**, 2041 (2007), proceedings of the 17^{th} International Conference on Magnetism.

[240] Y. Gaididei, D. D. Sheka, and F. G. Mertens, Appl. Phys. Lett. **92**, 012503 (2008).

[241] B. C. Choi, J. Rudge, E. Girgis, J. Kolthammer, Y. K. Hong, and A. Lyle, Appl. Phys. Lett. **91**, 022501 (2007).

[242] A. Barman, J. Phys. D: Appl. Phys. **43**, 195002 (2010).

[243] K. M. Lebecki, M. J. Donahue, and M. W. Gutowski, J. Phys. D: Appl. Phys. **41**, 175005 (2008).

[244] W. Wang, C. Mu, B. Zhang, Q. Liu, J. Wang, and D. Xue, Comput. Mater. Sci. **49**, 84 (2010).

[245] M. Grimsditch, L. Giovannini, F. Montoncello, F. Nizzoli, G. K. Leaf, and H. G. Kaper, Phys. Rev. B **70**, 054409 (2004).

[246] J. Fidler and T. Schrefl, J. Phys. D: Appl. Phys. **33**, R135 (2000).

[247] M. Donahue and R. McMichael, IEEE Trans. Magn. **43**, 2878 (2007).

[248] J. Miltat and M. Donahue, "Handbook of magnetism and advanced magnetic materials," (Wiley-Interscience, Chichester, 2007) Chap. Numerical Micromagnetics: Finite Difference Methods, pp. 742–764.

[249] W. Brown, *Micromagnetics* (Interscience Publishers, 1963).

[250] M. Donahue and D. G. Porter, *OOMMF User's Guide, Version 1.0* (Tech. Rep. NIS–TIR 6376, National Institute of Standards and Technology, Gaithersburg, MD, 1999) http://math.nist.gov/oommf/doc/userguide12a3/userguide/ .

[251] M. J. Donahue, D. G. Porter, R. D. McMichael, and J. Eicke, J. Appl. Phys. **87**, 5520 (2000).

[252] M. J. Donahue, J. Appl. Phys. **83**, 6491 (1998).

[253] M. J. Donahue and R. D. McMichael, Physica B: Cond. Matter **233**, 272 (1997).

[254] T. G. Stockham, Jr., in *Proceedings of the April 26-28, 1966, Spring Joint Computer Conference*, AFIPS '66 (Spring) (ACM, New York, NY, USA, 1966) pp. 229–233.

[255] K. Y. Guslienko and A. N. Slavin, Phys. Rev. B **72**, 014463 (2005).

[256] G. Rado and J. Weertman, Journal of Physics and Chemistry of Solids **11**, 315 (1959).

[257] B. Delaunay, Bull. Acad. Sci. USSR, Classe Sci. Mat. Nat. **7**, 793 (1934).

[258] W. Scholz, *Scalable Parallel Micromagnetic Solvers for Magnetic Nanostructures*, Ph.D. thesis, Institut für Festkörperphysik (2003).

[259] V. Kruglyak and R. Hicken, J. Magn. Magn. Mater. **306**, 191 (2006).

[260] M. Dvornik and V. V. Kruglyak, Phys. Rev. B **84**, 140405 (2011).

[261] A. V. Oppenheim and R. W. Schafer, *Discrete-Time Signal Processing* (Pearson Education, 2006).

[262] D. Kumar, O. Dmytriiev, S. Ponraj, and A. Barman, J. Phys. D: Appl. Phys. **45**, 015001 (2012).

[263] R. Lyons, *Understanding Digital Signal Processing*, Prentice-Hall accounting series (Pearson Education, 2010).

[264] F. Harris, *Multirate signal processing for communication systems* (Prentice Hall PTR, 2004).

[265] J. W. Cooley and J. W. Tukey, Math. Comp. **19**, 297 (1965).

[266] S. Neusser, B. Botters, M. Becherer, D. Schmitt-Landsiedel, and D. Grundler, Appl. Phys. Lett. **93**, 122501 (2008).

[267] F. S. Ma, H. S. Lim, Z. K. Wang, S. N. Piramanayagam, S. C. Ng, and M. H. Kuok, Appl. Phys. Lett. **98**, 153107 (2011).

[268] D. Stancil, *Theory of Magnetostatic Waves* (Springer-Verlag, 1993).

[269] R. Damon and J. Eshbach, J. Phys. Chem. Solids **19**, 308 (1961).

[270] K. Di, H. S. Lim, V. L. Zhang, M. H. Kuok, S. C. Ng, M. G. Cottam, and H. T. Nguyen, Phys. Rev. Lett. **111**, 149701 (2013).

[271] K.-S. Lee, D.-S. Han, and S.-K. Kim, Phys. Rev. Lett. **111**, 149702 (2013).

[272] H. Puszkarski, Surf. Sci. Rep. **20**, 45 (1994).

[273] S. Mamica, H. Puszkarski, and J. C. S. Lévy, Phys. Status Solidi B **218**, 561 (2000).

[274] C. Yu, M. J. Pechan, W. A. Burgei, and G. J. Mankey, J. Appl. Phys. **95**, 6648 (2004).

[275] R. D. McMichael and B. B. Maranville, Phys. Rev. B **74**, 024424 (2006).

[276] T. Fischbacher, M. Franchin, G. Bordignon, and H. Fangohr, IEEE Trans. Mag. **43**, 2896 (2007).

[277] J. W. Kłos, M. Krawczyk, and M. Sokolovskyy, J. Appl. Phys. **109**, 07D311 (2011).

[278] C. Costa, P. Barbosa, F. B. Filho, M. Vasconcelos, and E. Albuquerque, Solid State Commun. **150**, 2325 (2010).

[279] J. Kaczér and L. Murtinová, Phys. Status Solidi A **23**, 79 (1974).

[280] M. Sokolovskyy and M. Krawczyk, J. Nanopart. Res. **13**, 6085 (2011).

[281] T. Wolfram and R. E. De Wames, Phys. Rev. B **4**, 3125 (1971).

[282] C. A. F. Vaz, J. A. C. Bland, and G. Lauhoff, Rep. Prog. Phys. **71**, 056501 (2008).

[283] V. Vlaminck and M. Bailleul, Phys. Rev. B **81**, 014425 (2010).

[284] A. Christ, O. J. F. Martin, Y. Ekinci, N. A. Gippius, and S. G. Tikhodeev, Nano Lett. **8**, 2171 (2008), pMID: 18578551.

[285] Z. H. Cho and J. H. Yi, Concepts Magn. Reson. **7**, 95 (1995).

[286] R. Gieniusz, H. Ulrichs, V. D. Bessonov, U. Guzowska, A. I. Stognii, and A. Maziewski, Appl. Phys. Lett. **102**, 102409 (2013).

[287] T. G. Pedersen, C. Flindt, J. Pedersen, N. A. Mortensen, A.-P. Jauho, and K. Pedersen, Phys. Rev. Lett. **100**, 136804 (2008).

[288] J. Bai, X. Zhong, S. Jiang, Y. Huang, and X. Duan, Nat. Nanotechnol. **5**, 190 (2010).

[289] W. Oswald and Z. Wu, Phys. Rev. B **85**, 115431 (2012).

[290] H. Al-Wahsh, A. Akjouj, B. Djafari-Rouhani, and L. Dobrzynski, Surf. Sci. Rep. **66**, 29 (2011).

[291] B. Obry, P. Pirro, T. Brächer, A. V. Chumak, J. Osten, F. Ciubotaru, A. A. Serga, J. Fassbender, and B. Hillebrands, Appl. Phys. Lett. **102**, 202403 (2013).

[292] V. S. Tkachenko, A. N. Kuchko, M. Dvornik, and V. V. Kruglyak, Appl. Phys. Lett. **101**, 152402 (2012).

[293] Q. Wang, Z. Zhong, L. Jin, X. Tang, F. Bai, H. Zhang, and G. S. Beach, J. Magn. Magn. Mater. **340**, 23 (2013).

[294] J. Li, L. Zhou, C. T. Chan, and P. Sheng, Phys. Rev. Lett. **90**, 083901 (2003).

[295] C. Croënne, E. J. S. Lee, H. Hu, and J. H. Page, AIP Advances **1**, 041401 (2011).

[296] N. I. Polushkin, J. Appl. Phys. **114**, 033908 (2013).

[297] B. Hillebrands and K. Ounadjela, *Spin Dynamics in Confined Magnetic Structures I*, Anglistische Forschungen (Springer, 2002).

[298] H. Yang, G. Yun, and Y. Cao, J. Phys. D: Appl. Phys. **44**, 455001 (2011).

[299] J. Ding, M. Kostylev, and A. O. Adeyeye, Appl. Phys. Lett. **100**, 073114 (2012).

[300] G. Gubbiotti, S. Tacchi, M. Madami, G. Carlotti, S. Jain, A. O. Adeyeye, and M. P. Kostylev, Appl. Phys. Lett. **100**, 162407 (2012).

[301] M. Dvornik, Y. Au, and V. Kruglyak, in *Magnonics*, Topics in Applied Physics, Vol. 125, edited by S. O. Demokritov and A. N. Slavin (Springer Berlin Heidelberg, 2013) p. 101.

[302] A. Jafarpour, C. Reinke, A. Adibi, Y. Xu, and R. K. Lee, IEEE J. Quant. Electron. **40**, 1060 (2004).

[303] V. V. Kruglyak, P. S. Keatley, A. Neudert, R. J. Hicken, J. R. Childress, and J. A. Katine, Phys. Rev. Lett. **104**, 027201 (2010).

[304] C. Luo, S. G. Johnson, J. D. Joannopoulos, and J. B. Pendry, Phys. Rev. B **65**, 201104 (2002).

[305] S. Enoch, G. Tayeb, and B. Gralak, IEEE Trans. Antennas. Propag. **51**, 2659 (2003).

[306] X.-F. Li, X. Ni, L. Feng, M.-H. Lu, C. He, and Y.-F. Chen, Phys. Rev. Lett. **106**, 084301 (2011).

[307] R. Bali, M. Kostylev, D. Tripathy, A. O. Adeyeye, and S. Samarin, Phys. Rev. B **85**, 104414 (2012).

[308] S. Neusser, G. Duerr, S. Tacchi, M. Madami, M. L. Sokolovskyy, G. Gubbiotti, M. Krawczyk, and D. Grundler, Phys. Rev. B **84**, 094454 (2011).

[309] R. Leite and R. C. Filho, J. Magn. Magn. Mater. **226-230**, 482 (2001).

[310] M. Hurben and C. Patton, J. Magn. Magn. Mater. **139**, 263 (1995).

[311] X.-Y. Jiang, ed., "Metamaterial," (Intech, 2012) Chap. Magnonic Metamaterials, pp. 341–371.

[312] M. Mruczkiewicz, M. Krawczyk, R. V. Mikhaylovskiy, and V. V. Kruglyak, Phys. Rev. B **86**, 024425 (2012).

[313] R. Zivieri and L. Giovannini, Metamaterials **6**, e127 (2012).

[314] O. Dmytriiev, M. Dvornik, R. V. Mikhaylovskiy, M. Franchin, H. Fangohr, L. Giovannini, F. Montoncello, D. V. Berkov, E. K. Semenova, N. L. Gorn, A. Prabhakar, and V. V. Kruglyak, Phys. Rev. B **86**, 104405 (2012).

[315] B. Rana, D. Kumar, S. Barman, S. Pal, Y. Fukuma, Y. Otani, and A. Barman, ACS Nano **5**, 9559 (2011).

[316] V. Veerakumar and R. E. Camley, Phys. Rev. B **74**, 214401 (2006).

[317] M. P. Kostylev, A. A. Serga, and B. Hillebrands, Phys. Rev. Lett. **106**, 134101 (2011).

[318] D. Alleyne and P. Cawley, J. Acoust. Soc. Am. **89**, 1159 (1991).

[319] G. Burt, S. V. Samsonov, K. Ronald, G. G. Denisov, A. R. Young, V. L. Bratman, A. D. R. Phelps, A. W. Cross, I. V. Konoplev, W. He, J. Thomson, and C. G. Whyte, Phys. Rev. E **70**, 046402 (2004).

[320] H. Gersen, T. J. Karle, R. J. P. Engelen, W. Bogaerts, J. P. Korterik, N. F. van Hulst, T. F. Krauss, and L. Kuipers, Phys. Rev. Lett. **94**, 073903 (2005).

[321] K. Sekiguchi, T. N. Vader, K. Yamada, S. Fukami, N. Ishiwata, S. M. Seo, S. W. Lee, K. J. Lee, and T. Ono, Appl. Phys. Lett. **100**, 132411 (2012).

[322] E. Lewis, M. Faraday, J. Kerr, and P. Zeeman, *The Effects of a Magnetic Field on Radiation: Memoirs by Faraday, Kerr, and Zeeman*, Scientific memoirs, VIII (American Book Company, 1900).

[323] Spectra-Physics, *Model 3980: Frequency Doubler and Pulse Selector* (Spectra–Physics, California, 2002).

[324] B. Rana, D. Kumar, S. Barman, S. Pal, R. Mandal, Y. Fukuma, Y. Otani, S. Sugimoto, and A. Barman, J. Appl. Phys. **111**, 07D503 (2012).

[325] B. K. Mahato, B. Rana, R. Mandal, D. Kumar, S. Barman, Y. Fukuma, Y. Otani, and A. Barman, Appl. Phys. Lett. **102**, 192402 (2013).

[326] D. Kumar, J. W. Kłos, M. Krawczyk, and A. Barman, J. Appl. Phys. **115**, 043917 (2014).

[327] M. Kammerer, M. Weigand, M. Curcic, M. Noske, M. Sproll, A. Vansteenkiste, B. Van Waeyenberge, H. Stoll, G. Woltersdorf, C. H. Back, and G. Schuetz, Nat. Commun. **2**, 279 (2011).

[328] S. Yakata, M. Miyata, S. Honda, H. Itoh, H. Wada, and T. Kimura, Appl. Phys. Lett. **99**, 242507 (2011).

[329] M. Jaafar, R. Yanes, D. Perez de Lara, O. Chubykalo-Fesenko, A. Asenjo, E. M. Gonzalez, J. V. Anguita, M. Vazquez, and J. L. Vicent, Phys. Rev. B **81**, 054439 (2010).

[330] B. Pigeau, G. de Loubens, O. Klein, A. Riegler, F. Lochner, G. Schmidt, and L. W. Molenkamp, Nat. Phys. **7**, 26 (2011).

[331] M. Curcic, H. Stoll, M. Weigand, V. Sackmann, P. Juellig, M. Kammerer, M. Noske, M. Sproll, B. Van Waeyenberge, A. Vansteenkiste, G. Woltersdorf, T. Tyliszczak, and G. Schütz, Phys. Status Solidi B **248**, 2317 (2011).

[332] S. Jain, V. Novosad, F. Fradin, J. Pearson, V. Tiberkevich, A. Slavin, and S. Bader, Nat. Commun. **3**, 1330 (2012).

[333] X. Zhu, Z. Liu, V. Metlushko, P. Grütter, and M. R. Freeman, Phys. Rev. B **71**, 180408 (2005).

[334] K. S. Buchanan, P. E. Roy, M. Grimsditch, F. Y. Fradin, K. Y. Guslienko, S. D. Bader, and V. Novosad, Nat. Phys. **1**, 172 (2005).

[335] A. D. Belanovsky, N. Locatelli, P. N. Skirdkov, F. A. Araujo, J. Grollier, K. A. Zvezdin, V. Cros, and A. K. Zvezdin, Phys. Rev. B **85**, 100409 (2012).

[336] C. E. Zaspel, Appl. Phys. Lett. **102**, 052403 (2013).

[337] K. Y. Guslienko, K. S. Buchanan, S. D. Bader, and V. Novosad, Appl. Phys. Lett. **86**, 223112 (2005).

[338] K. S. Buchanan, M. Grimsditch, F. Y. Fradin, S. D. Bader, and V. Novosad, Phys. Rev. Lett. **99**, 267201 (2007).

[339] A. A. Thiele, J. Appl. Phys. **45**, 377 (1974).

[340] N. K. Bajaj, *The Physics of Waves and Oscillations* (Tata McGraw - Hill, 1988).

[341] T. Kanna and M. Lakshmanan, Phys. Rev. Lett. **86**, 5043 (2001).

[342] D.-S. Han, A. Vogel, H. Jung, K.-S. Lee, M. Weigand, H. Stoll, G. Schutz, P. Fischer, G. Meier, and S.-K. Kim, Sci. Rep. **3**, 2262 (2013).

[343] T. F. Bogart, "Electronic devices and circuits," (Universal Book Stall, New Delhi, New Delhi, 2000) Chap. 5, pp. 134 – 195.

[344] R. L. Compton and P. A. Crowell, Phys. Rev. Lett. **97**, 137202 (2006).

[345] J. Volz and A. Rauschenbeutel, Science **341**, 725 (2013).

[346] A. J. Bourdillon, G. P. Williams, Y. Vladimirsky, and C. B. Boothroyd, Proc. SPIE **5374**, 546 (2004).

List of Corrections

1: In Chap. 11, titled 'Experimentation Involving Magnonic Antidot Waveguides,' I demonstrate that some of the theoretical observations made in the thesis can be validated experimentally. I also note that samples are difficult to fabricate with high precision on the considered length-scales and conclude in **Sec. 11.4 Conclusions (Page 165)**, that advances in fabrication procedures are needed in order to readily create reliable magnonic devices. In light of review comments, the following statement has also been added to the section: "Alternatively, computational methods may be improved upon so that samples which can be fabricated readily are simulated in a reasonable amount of time."

2: **On page 53: Sub–Section 3.5.2**: I stated, "Thus, photolithography should be used to etch micron sized vast regions, while FIB milling should be used where resolution is below 50 nm. Anything in between those limits may be handled using e–beam lithography." As pointed out in a review comment, these statements are confessedly misleading. They have been replaced with the following: "Both photolithography and e-beam lithography are used to define patterns on resist followed by deposition of materials and subsequent lift–off process, or dry or wet etching. On the other hand focused ion beam is used to directly mill out materials with high precision. Hence, photolithography and subsequent lift–off or etching may be used to create micrometer and sub–micrometer sized structures, while e–beam lithography and lift–off or etching or focused ion beam milling may be used for creating sub–100 nm structures."